Historical surface mass balance reconstruction 1984 – 2017 from GreenTrACS multi-offset ground-penetrating radar

Tate G. MEEHAN,[1,2] H.P. MARSHALL,[1,2] John H. BRADFORD,[3] Robert L. HAWLEY,[4] Thomas B. OVERLY,[5,6] Gabriel LEWIS,[4] Karina GRAETER,[4] Erich OSTERBERG,[4] Forrest McCARTHY [4]

[1]*Department of Geoscience, Boise State University, Boise, ID, USA*

[2] *U.S. Army Cold Regions Research and Engineering and Laboratory, Hanover, NH, USA*

[3]*Department of Geophysics, Colorado School of Mines, Golden, CO, USA*

[4]*Department of Earth Sciences, Dartmouth College, Hanover, NH, USA*

[5]*Cryospheric Sciences Lab, NASA Goddard Space Flight Center, Greenbelt, MD, USA*

[6]*Earth System Science Interdisciplinary Center, University of Maryland, College Park, MD, USA*

Correspondence: Tate Meehan <tatemeehan@u.boisestate.edu>

ABSTRACT. We present a multi-channel, multi-offset, ground-penetrating radar method that makes continuous estimates of snow and firn density, layer depth, and accumulation. Our method uses the electromagnetic velocity, estimated from waveform travel-times measured at common-midpoints between sources and receivers. Previously, common-midpoint radar experiments on ice sheets have been limited to point observations. We completed radar velocity analysis in the upper $\sim 2\ m$ to estimate the surface and average snow density of the Greenland Ice Sheet. We paramterized the Herron and Langway (1980) firn density and age model using the radar-derived snow density, radar-derived SMB $(2015 - 2017)$, and reanalysis-derived temperature data. We applied structure-oriented filtering to the radar image along constant age horizons and increased the depth at which horizons could

be reliably interpreted. We reconstructed the historical instantaneous surface mass balance, which we averaged into annual and multidecadal products along a 78 km traverse for the period $1984-2017$. We found good agreement between our physically constrained parameterization and a firn core collected from the dry snow accumulation zone, and gained insights into the spatial correlation of surface snow density.

1. INTRODUCTION

The Greenland Ice Sheet (GrIS) expresses high variability in ice loss, and hence sea level rise, due to the regional scale variability in the processes governing mass balance (Lenaerts and others, 2019). Surface mass balance (SMB) continues to be the dominant contributor of GrIS mass loss, but ice sheet wide SMB simulated from regional climate models maintains $\sim 25\%$ uncertainty (Shepherd and others, 2020). Efforts to improve SMB simulation (e.g. Fettweis and others, 2017) are limited by the scarcity of observations, which are required to evaluate the model performance (e.g Noël and others, 2016). Traditionally, SMB measurements are made at the point scale during infrequent field efforts, through the laborious process of excavating snow pits or drilling firn cores. The sparseness of snow pit observations on the GrIS limits the testable correlation lengths and tends to debilitate spatial correlation analysis. Consequentially, surface density measurements have shown no spatial correlation over length scales of tens to hundreds of kilometers (Fausto and others, 2018). Due to the unknown variability of density and SMB, point measurements used to parameterize a firn model (e.g. Zwally and Li, 2002) must be extrapolated to regional scales cautiously. In space borne altimetry retrievals of GrIS mass balance, the uncertainty in modeled corrections for snow densification required to convert a measured change in ice sheet volume to a change in mass causes $\sim 16\%$ uncertainty (Shepherd and others, 2020).

Ground-penetrating radar (GPR) surveys are capable of imaging layers of accumulated snow (e.g. Vaughan and others, 1999). However, conventional, single-offset GPR analysis requires an independent measurement of firn density to estimate the accumulation (Navarro and Eisen, 2009). Point SMB measurements often provide the required density information to extrapolate the density profile along the track of the radar sounding (e.g. Hawley and others, 2014; Overly and others, 2016). Yet, relying on sparse firn cores to extrapolate density over tens to hundreds of kilometers may bias the derived accumulation estimates. For example, ice lenses sampled in a firn core increase the average density and can be incorrectly extrapolated over tens of kilometers, as these features are uncorrelated over tens of meters (Brown and others, 2011). For the period 1971 – 2016, greater than 10% bias to the SMB is possible, when firn cores are not available for extrapolation (Lewis and others, 2019). Inaccuracies are greater in southern Greenland, which is experiencing greater near surface firn densification as a result of atmospheric warming (Graeter and others, 2018), than in central Greenland. Parameterization of snow and firn densification continues to improve (e.g. Meyer and others, 2020); yet, evolving the firn using full energy balance modeling remains operationally challenging and is limited spatially by the unknown heterogeneities of surface snow density, accumulation, and melt (Vandecrux and others, 2018). Surface snow density parameterizations formulated around temperature and wind speed (e.g van Kampenhout and others, 2017), are arguably less preferable than density measurements because of uncertainties in estimating wind speed and modeling the unknown length scale variability that exists in the GrIS snow (Fausto and others, 2018).

Radar retrievals of snow density are an appealing alternative to *in situ* observations of snow and firn because the methods are nondestructive and rapidly acquire vast amounts of data. However, few methods for continuously mapping snow and firn density exist (e.g. Grima and others, 2014) due to the complexities of data inversion. In this work we present the analysis of multi-channel, multi-offset, radar (MxRadar) imagery along a 78 km traverse in the GrIS dry snow accumulation zone to demonstrate the capability of this method, which has the advantage of ascertaining snow and firn density, and depth, and thereby SMB, independently. Borrowing from exploration geophysics, we developed the MxRadar workflow on the analysis of the radar surface wave, which exhibits linear moveout (LMO), and the fall 2014 isochronous reflection horizon (IRH) to estimate the surface snow density, column average density, horizon depth, and 2015 – 2017 SMB. Additionally, we show how well these radar-derived observations can be directly used as input to the Herron and Langway (1980) firn density and age model. We use the firn model to further enhance the MxRadar imagery and extend the historical period of the SMB reconstruction to 1984 – 2017 with instantaneous ($\sim$ 14 days) temporal intervals. We compare the resulting SMB against a firn core and quantify the length of spatial correlation that exists in surface snow density. We quantify the bias reduction in SMB derived using the measured-modeled, MxRadar–Herron and Langway (1980) method. Then we provide a discussion of the results, limitations and advantages of the method, and future directions.

2. GREENLAND TRAVERSE FOR ACCUMULATION AND CLIMATE STUDIES

The Greenland Traverse for Accumulation and Climate Studies (GreenTrACS) is a multi-disciplinary study of recent SMB changes in the West Central percolation and dry snow accumulation zones of the GrIS.

During the Spring of 2016 and 2017 we traveled a total of 4436 km by snowmobile from Raven/DYE-2 to Summit Station along the elevation contour straddling the percolation zone, and along West-East "spurs" perpendicular to the elevation contours. Throughout the expedition we collected 16 shallow ($22-32$ m) firn cores and dug 42 snow pits; 16 pits were coincident with the cores and the 26 others were dug at the ends of the spurs (Fig. 1 and Fig. 2). Our GreenTrACS field seasons occurred prior to the on-set of melt to reduce the complexity of radar data inversion. The cores and the coincident snow pits were sampled for density, isotopic chemistry, dust, and trace elements to define annual layer depths for measuring SMB (e.g. Graeter and others, 2018; Lewis and others, 2019). As firn cores are strategically located point measurements, GPR imagery is often leveraged to spatially extend the record of firn stratigraphy between core sites for accumulation studies (Spikes and others, 2004; Hawley and others, 2014; Lewis and others, 2019). We operated a suite of radar instruments spanning the frequency range $0.4-18$ GHz; the focus of this study is the MxRadar.

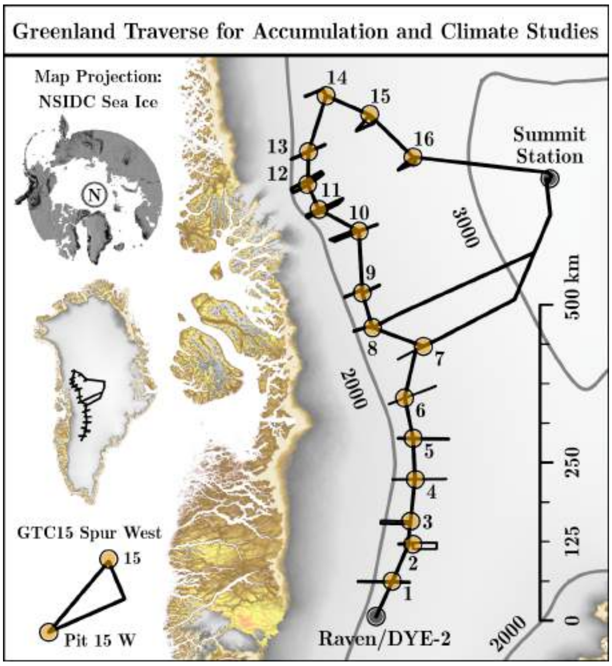

Fig. 1: GreenTrACS firn cores (GTCs) are numbered $1-16$. Ground-penetrating radar surveys were conducted along spur traverses and the main route that links the GTCs. We developed our radar processing and analyses at GTC15 Spur West (lower left inset). The 2000 m asl contour envelopes the western spurs. Surface elevation was acquired from Morlighem (2017) and Porter and others (2018).

2.1. Study Area

GreenTrACS Core 15 (GTC15) is the second most northern core site of the GreenTrACS campaign ($47.197°W$, $73.593°N$) and is ~ 2600 m above sea level. GTC15 had an average annual temperature of -25.7 ± 1.0 $°C$ (*Modern-Era Retrospective analysis for Research and Applications* (MERRA), 1979-2012), and an average annual SMB of 0.306 ± 0.021 $m\ w.e.\ a^{-1}$ (1969-2016). The site experiences little to no melt, measured as the average melt feature percentage determined by normalizing each year's ice layer water equivalent by the annual water equivalent and then averaging (0.47%, 1969-2016).

GTC15 Spur West is a triangular, clockwise circuit that departs from and returns to GTC15 (Fig. 1 inset). The first of three transects is 15 km in length with the bearing 157° which begins at GTC15, the second transect is 30 km in length at 246.5° which ends at Pit 15 W, and the final transect is 33 km in length from Pit 15 W to GTC15 with the bearing 40.5°. The GrIS surface of GTC15 Spur West was wind affected snow with sastrugi $\lessapprox 25$ cm in height. The cyclicity in the topographic profile (Fig. 2) results from our return to GTC15 along a path oblique to the path approaching Pit 15 W. The SMB changes significantly across the $\lessapprox 5$ km wide trough between distances $40 - 50$ km. We selected this particular spur to develop our processing and analyses because of the apparent interplay between the surface elevation, SMB, and heterogeneous layering observed in the radar imagery.

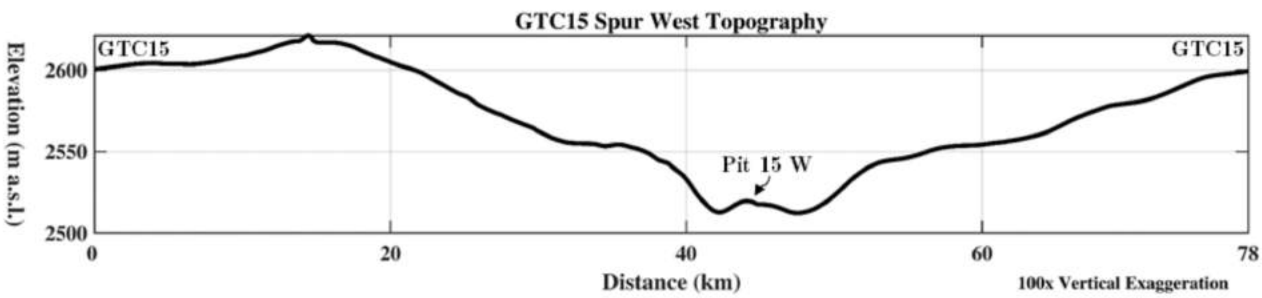

Fig. 2: Topographic profile of GreenTrACS Core 15 Spur West. The topographic undulation near Pit 15 W is responsible for increases and decreases in accumulation.

2.2. Field Methods

The MxRadar is a Sensors & Software 500 MHz GPR deployed with a multi-channel adapter in a multi-offset configuration using three transmitting and three receiving antennas (Fig. 3). During data acquisition, the transmitting and receiving channels were multiplexed to form nine radargrams which have independent antenna separations (offsets). The antennas were co-polarized, perpendicular to the direction of travel, and all are specified at 500 MHz with greater than two octave bandwidth. However, dependent on the antenna pairing, the actual central frequency and bandwidth varied on the order of tens of MHz. Of the previous studies applying GPR velocity analysis, none have performed continuous estimates throughout tens of kilometers distance. Our methods and analysis are tailored to produce meaningful data for the evaluation and improvement of snow cover and firn models and regional climate and reanalysis modeling of SMB.

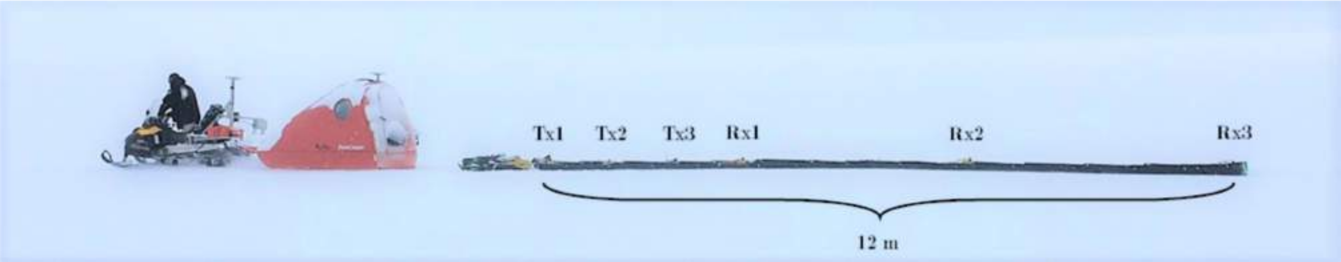

Fig. 3: The MxRadar streamer array has three transmitting (Tx) and three receiving (Rx) antennas, which form nine independent offsets that were linearly spaced from $1.33-12\ m$ apart. We simultaneously acquired nine continuous radargrams (one for each constant offset) and then binned the source-receiver pairs into common-midpoint (CMP) gathers.

3. ANALYSIS METHODS

We review multi-offset GPR methods for SMB calculations to clarify the advantages of the multi-offset technique that are also important for interpreting the results in Section 3.1. Much of the methodological detail can be found in the Supplementary Material S.1. Here, we touch on the methodology to simplify our strategy for reconstructing the historical SMB for the period 1984 – 2017 along GTC15 Spur West. We consider SMB rather than the accumulation rate because of unaccounted mass lost to sublimation and ablation. SMB is conventionally measured using GPR by interpreting a select few IRHs using a constant age interval and applying the average normalized firn density over this interval (e.g. Lewis and others, 2019). Instead, we rely on the models of density and age, which are discretized in depth at a comparable resolution to the GPR data, to generate a SMB model with instantaneous ($\sim$ 14 day) temporal intervals (Section S.1.3). We average annual SMB from many realizations of the instantaneous SMB model in a Monte Carlo simulation to assess uncertainty (Section S.1.4). We estimate the multidecadal average SMB, invoking the central limit theorem, by repeatedly drawing from 10 of the 33 annual SMB distributions at random and averaging.

To parameterize the firn model, we first complete conventional signal processing on the nine radargrams, which consists of a two octave bandpass filter around 500 MHz, amplitude gain corrections for wavefront spreading, coherent noise removal (background subtraction), and random noise removal (smoothing). Then we interpret the air wave, surface wave, and a shallow reflection (Fig. 4) on each of the nine images using a semi-automatic picking algorithm (Section S.1.1). We invert the travel-times of the surface wave and the shallow reflection (see section 3.1.1) to estimate the average electromagnetic (EM) propagation velocity and depth of the dry snow and firn in a least-squares approach (Section S.1.2), which uses random resampling of the data to estimate uncertainties (Section S.1.4). We then apply a petrophysical model (Wharton and others, 1980) which relates the EM velocity of dry snow and firn to its density (Section S.1.3).

Our measured-model approach relies on the Herron and Langway (1980) empirical firn density and age model, hereafter HL, which requires three input parameters: average snow density, average annual accumulation, and 10 m firn temperature. We parameterized the HL model with the MxRadar snow density, MxRadar SMB ($2015-2017$), and MERRA 2 m air temperature as a proxy for firn temperature (Loewe, 1970), to model the stratigraphic age and density of the firn. We assessed the firn model accuracy and sensitivity to parameterization to illustrate the accuracy of the MxRadar-HL (MxHL) firn density (Section S.1.5). We justify tuning the age model to improve our estimates of SMB in a process that jointly updates the age-depth and SMB models according to the radiostratigraphy.

The age model allows us to convert the time domain radar image into the stratigraphic age domain, known as the Wheeler (1958) domain. In principle, the firn structure can be estimated by the age model because the statrigraphy is deposited in isochronous layers. The imaged firn structure can be flattened by converting the time domain GPR image into the Wheeler domain because the rows of the Wheeler image maintain a constant age. We ensure the relative structure of the age model by picking five horizons of the Wheeler transformed radiostragraphy with an average epoch of 5.3 ± 2.7 years (the latest being the 1991 horizon) and perturbing the age model with the interpolated residuals to re-flatten the Wheeler image. We developed a structure-oriented noise-suppression filter which operates along the radar reflection horizons in the Wheeler domain to eliminate remnant noise after conventional GPR signal processing (Section S.1.6). This innovative signal processing technique allows SMB estimates to depths at which previously the stratigraphy was uninterpretable due to the low signal-to-noise ratio. We then convert the filtered radargram from the Wheeler domain into the depth domain and interpret 16 IRHs with an average epoch of 2.1 ± 1.7 years dating back to 1984. We calculate the error between the GTC15 geochemically determined age-depth scale and the 16 picked IRHs and interpolate a second grid of perturbations which we applied as a final update to the age model. We calculate the instantaneous SMB by taking a numerical derivative of the age-depth model $\left(\frac{\mathrm{d}z}{\mathrm{d}a}\right)$ and multiplying it by the MxHL density model (Eq. (S.12)).

3.1. Review of Multi-offset Radar

Common-midpoint (CMP) radar surveys are practiced in glaciology to estimate the EM wave speed of the ice, air, and/or water mixture (e.g. Eisen and others, 2002). The wave speed is related to firn density and liquid water content using a dielectric mixture formula for a two or three phase relationship (e.g. Looyenga, 1965; Wharton and others, 1980). In most studies, the CMP survey is treated as a point measurement of the firn vertical density profile, which is less laborious than extracting a core, but offers less vertical resolution and accuracy. Prior to GreenTrACS, CMP experiments on ice sheets were limited to point observations. We synthesized continuous CMP data by towing a streamer of nine antenna pairs that were linearly spaced from $1.33 - 12$ m apart (Fig. 3). While the antenna pairs in this deployment do not have a common midpoint, we rebinned the constant offset radargrams for each pair independently, such that the analysis can be performed on offset gathers with common midpoints.

3.1.1. Interpreting the Near-surface Waves

Numerous geophysical methods exist for velocity analyses of CMP data gathers. Analyses of reflection data can be divided into two fundamental categories by the question, "Does the analysis assume normal moveout?" Normal moveout (NMO) is the reflection travel-time dependence on offset that arises from a homogenously-layered and planar subsurface structure (within the distance of the maximum antenna offset) that exhibits small vertical velocity heterogeneity (Al-Chalabi, 1974). Previous studies avoided classical NMO analysis, instead using less automated, more computationally expensive methods that favored accuracy (Bradford and others, 2009; Brown and others, 2012, 2017). Many caveats of NMO velocity analysis and sources of error in the radar common-midpoint analysis are discussed in Barrett and others (2007). We demonstrate that NMO analysis of the snow and shallow firn yields a satisfactory result for data with low noise (see supplement S.1.5), as ice sheet stratigraphy in the high elevation accumulation zone is close to homogeneous and planar at the length scale of the radar streamer array.

Linear moveout (LMO) is the one-way travel-time dependence on offset of radar waves traveling directly from the transmitter through the air and ice sheet surface to the receiver antenna. We assume that the air wave expresses the linear moveout velocity $c \approx 0.2998$ m/ns to calibrate the timing of the multi-channel system (Section S.1.2). To analyze the surface wave, we assume that the shallow, surficial snow is also planar and homogeneous at the scale of the maximum offset. We identify the air wave, surface wave, and a near surface reflection and their respective moveout behavior in Fig. 4. The travel-times of these waves were interpreted using a horizon tracking algorithm (see supplement S.1.1). The linear methods for LMO and NMO velocity analysis are described in Section S.1.2 and the methods for estimating the surficical and average snow density and depth of the fall 2014 IRH are discussed in Section S.1.3. We quantify the uncertainty of the density, depth, age, and SMB used to parameterize the HL model in Section S.1.4.

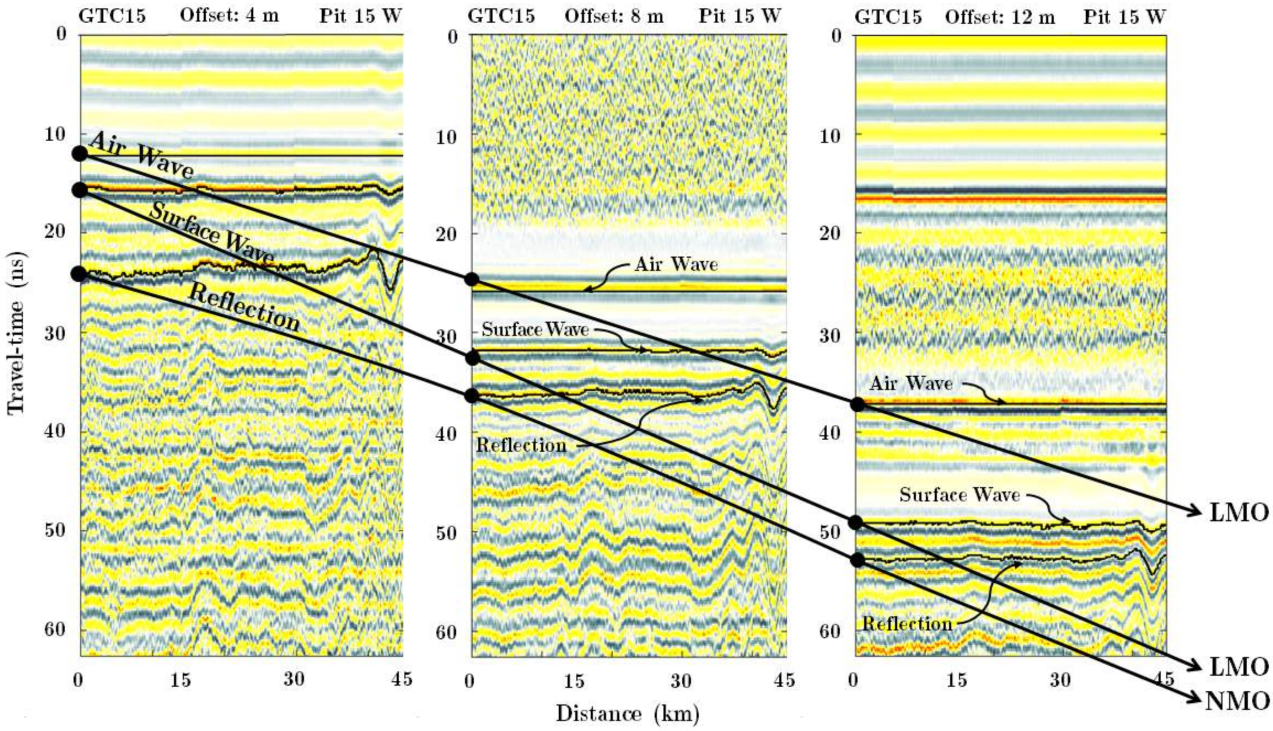

Fig. 4: This offset gather is represented by radargrams at offsets 4, 8, and 12 m from the initial 45 km of GTC15 Spur West, and is annotated to convey the waveforms used in our analysis and the concepts of normal moveout (NMO) and linear moveout (LMO). Consider the traces at zero distance for each offset as a CMP gather. The air wave and surface wave arrivals are modeled by a linear expression of travel-time as a function of offset (Eq. (S.1)). The air wave is the first to arrive and expresses a more shallow slope (faster velocity) than the surface wave which is impeded while traveling through the snow. The annotated reflection expresses nonlinear moveout which is approximated by NMO (Eq. (S.2)). The surface-wave (LMO) and reflection (NMO) annotated in this diagram are used to estimate the surface snow density, average snow density, and depth of the fall 2014 isochronous reflection horizon (IRH). The age of the horizon was determined at GTC15 and allowed us to estimate the 2015 – 2017 SMB (see supplement S.1.3), and in turn, is used to parameterize the HL model (see supplement S.1.5).

3.2. Spatial Correlation of Surface Snow Density

The LMO and NMO estimated snow densities are independent measurements of the of the snow density above the interpreted radar horizon. The GPR surface wave maintains a fairly consistent depth level (~ 0.5 m, Eq. (S.9)), but the NMO reflection horizon does not. To mitigate the effects of depth on the correlation we extracted the rows of the MxHL density model corresponding to the average depth of the LMO (0.5 m) and NMO (1.92 m) horizons interpreted for velocity analysis (Fig. 4). We used Pearson (1907) correlation to determine the relationship between the density at 0.5 m depth and the density at 1.92 m depth. Additionally, we conducted variogram analysis (Matheron, 1963) on the LMO estimated snow density for each of the three transects of GTC15 Spur West. We determined the length scale over which there is consistent spatial correlation of the surface snow density across all three transects as the distance where the three experimental variograms diverge.

4. RESULTS

The multi-offset radar travel-time inversion determined the GrIS surface snow density and average snow density without manual observations (Fig. 5). We estimated the 2015 − 2017 SMB from the MxRadar-derived snow depth and density using the GTC15 age of the near-surface IRH (Fig. 5). The LMO and NMO densities were independently estimated and strongly correlate ($R^2 = 0.67$, $p = 0$). Spatial patterns in the LMO derived snow density are consistent for three azimuths up to 2 km lag distance (Fig. 6).

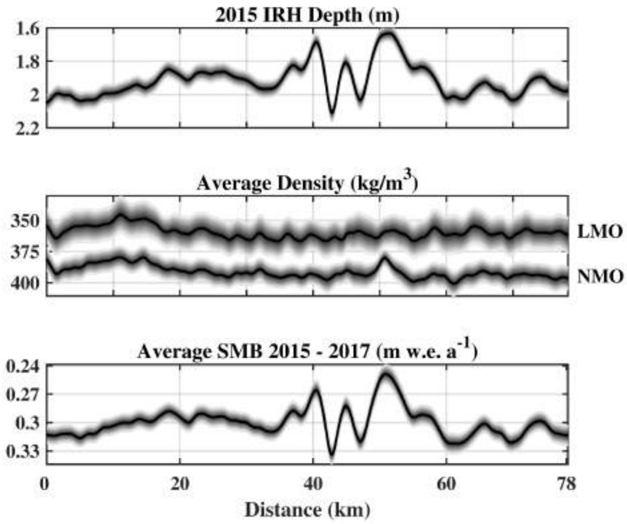

Fig. 5: The MxRadar inversion parameter distributions along GTC15 Spur West. The LMO and NMO densities were independently estimated and strongly correlate ($R^2 = 0.67$, $p = 0$). The MxHL model is parameterized by the average of the LMO and NMO densities, the 2015 − 2017 average SMB, and MERRA (1979 − 2012) average 2 m temperature.

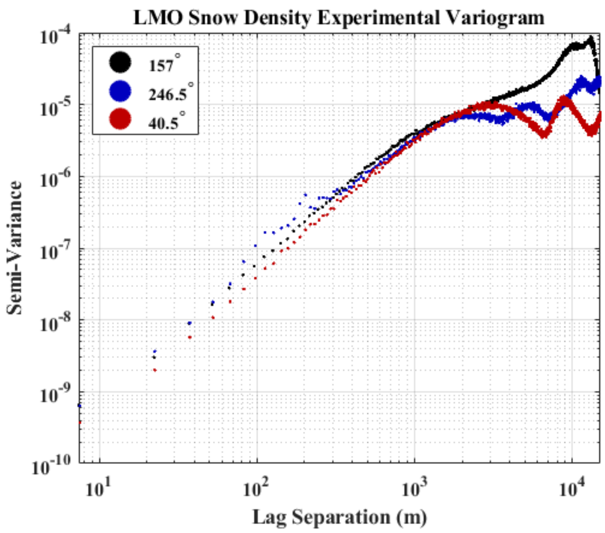

Fig. 6: We calculated experimental variograms of the LMO estimated snow density along the three azimuths of GTC 15 Spur West using lag separations up to 15 km. Plotted in log-log space, the linearity of each variogram slope indicates that spatial correlation exists up to ~ 2 km distance. Correlation beyond this distance is difficult to assess given the limited azimuths and lag separations possible for GTC 15 Spur West.

By combining the radar-derived density and SMB with MERRA 2 m temperature we accurately parameterized the HL firn density and age model. For depths up to ~ 22.5 m the mean absolute error between GTC15 densities and MxHL densities is 9.6 kg/m^3, with a bias of $\lessapprox 1$ kg/m^3, and rms error of 12.2 kg/m^3. We find that extrapolating the GTC15 densities along GTC15 Spur West introduces an insignificant (on the order of 1%) bias to the SMB of -0.004 m $w.e.$ a^{-1} and rms error of 0.005 m $w.e.$ a^{-1}. The MxHL firn model permitted radar imaging in the depth and stratigraphic age domains. In Fig. 7 and Fig. 8, we illustrate our structure-oriented filter along GTC15 Spur West between $35 - 55$ km distance, where the largest heterogeneity in firn stratigraphy occurs. After applying structure-oriented filtering, we were able to interpret significantly more IRHs and refine the age-depth model to an accuracy of ± 31 days (see supplement S.1.4).

We reconstructed the temporal SMB history from Jan. 1984 to Jan. 2017 and compare our result to the GTC15 firn core derived SMB in Fig. 9. The MxHL SMB history has a mean absolute error of 0.038 m $w.e.$ a^{-1}, a bias of 0.004 m $w.e.$ a^{-1}, and an rms error of 0.047 m $w.e.$ a^{-1}. Uncertainty in the SMB measured from GTC15 was calculated following Graeter and others (2018). Average uncertainty in annual SMB is 0.036 m $w.e.$ a^{-1} and 0.044 m $w.e.$ a^{-1} for MxHL and GTC15, respectively. The mean thickness of an annual layer for the period $1984-2017$ is 57.9 cm as measured at GTC15. The mean absolute error in the thickness of an annual layer estimated by MxHL is 7.8 cm, which contributes 0.039 m $w.e.$ a^{-1} (13%) error in the SMB reconstruction on average. Density inaccuracies in the SMB reconstruction result in a 0.004 m $w.e.$ a^{-1} (1.3%) error on average. The MxHL $1984 - 2017$ multidecadal average SMB is 0.297 ± 0.016 m $w.e.$ a^{-1} and is a good estimator of the GTC15 $1984 - 2017$ multidecadal average SMB (0.301 ± 0.025 m $w.e.$ a^{-1}). At GTC15 the $2015 - 2017$ average SMB is within the uncertainty bounds of the multidecadal averages spanning $1969 - 2017$, the oldest period spanned by the core, and $1984 - 2017$ the period spanned by the MxRadar imagery.

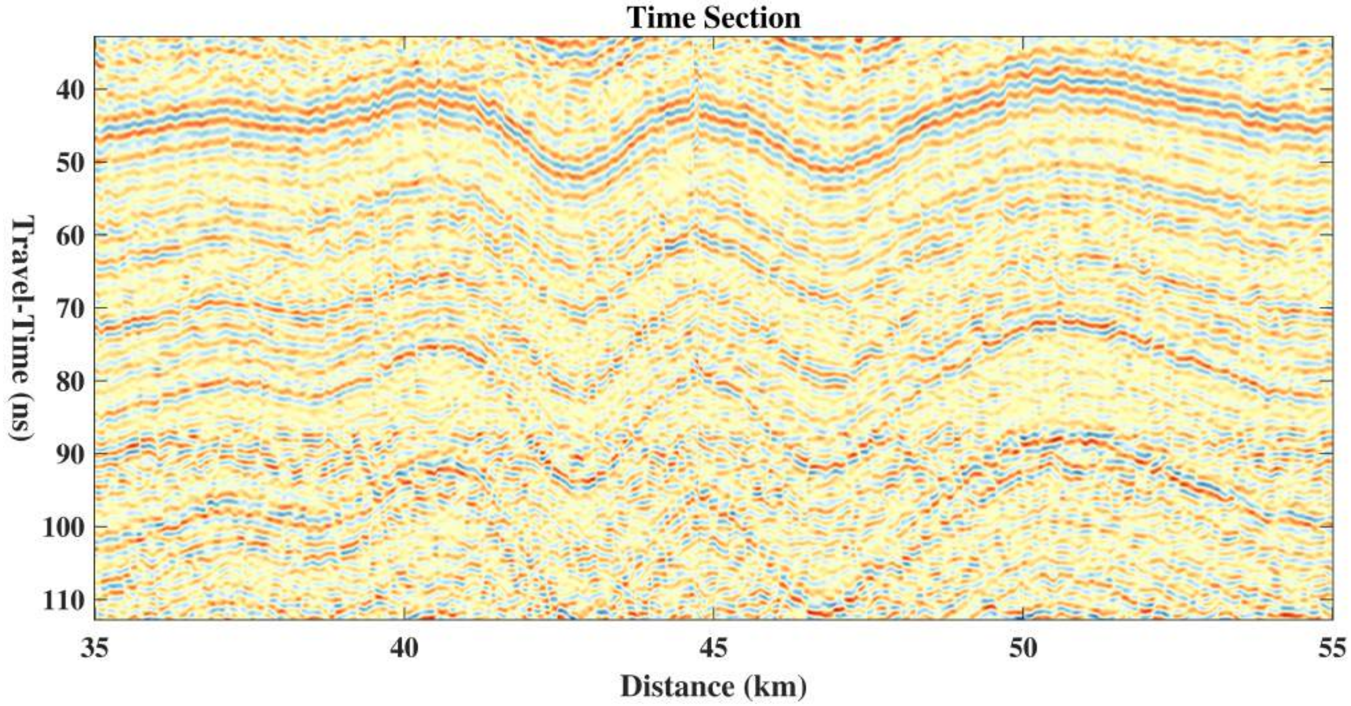

Fig. 7: Conventional GPR processing was applied to each of the nine constant offset radargrams. We then performed NMO correction to project each constant offset image to zero offset. We stacked the NMO corrected radargrams together to synthesize one conventional GPR travel-time image. The travel-time image remains quite noisy, and it is difficult to interpret due to the discontinuities along the reflection horizons.

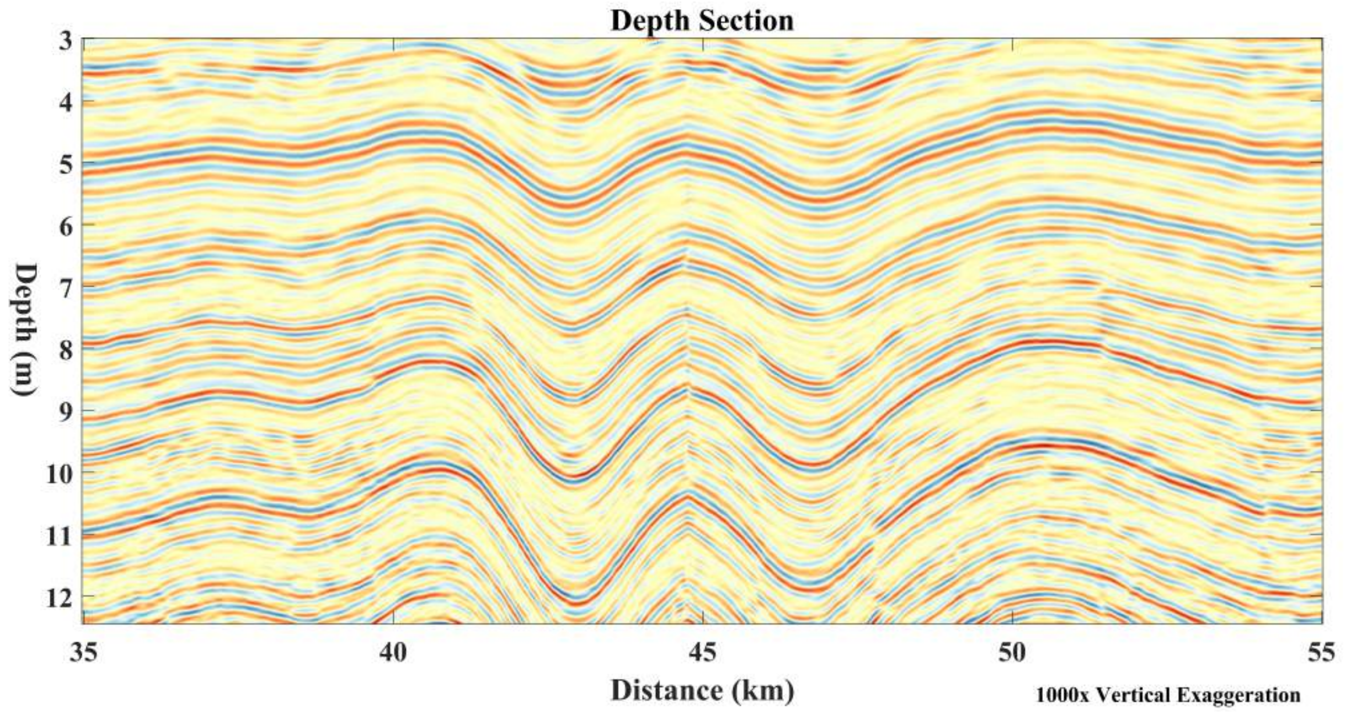

Fig. 8: The travel-time image (Fig. 7) is first transformed into the stratigraphic age domain, known as the Wheeler (1958) domain. Then we applied structure-oriented filtering to the Wheeler domain image and converted into the depth domain. The depth section, taken from GTC15 Spur West, has remarkable continuity along the reflection horizons, which allows us to interpret IRHs to $\sim 22.5\ m$ depth. The undulation in the firn stratigraphy is caused by spatial variablilty in snow accumulation. It is necessary to interpret along steeply varying undulations like these to evaluate high resolution ($< 5\ km$) regional climate model simulations of SMB. However, without the structure-oriented filter we would be unable to track the reflection horizons along the undulations.

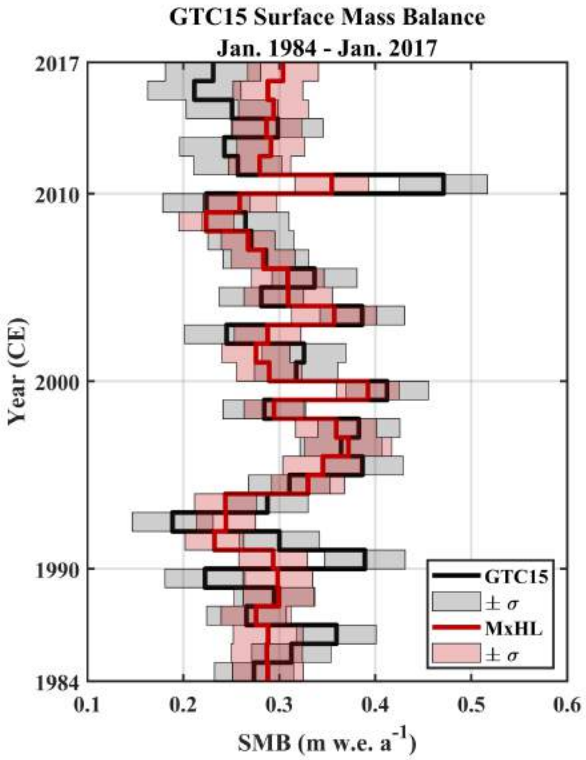

Fig. 9: The GTC15 and MxHL historical SMB for Jan. 1984 – Jan. 2017. Uncertainty in GTC15 SMB ($\pm\sigma$) was estimated following Graeter and others (2018). Uncertainties in the MxHL 1984 − 2017 SMB ($\pm\sigma$) were propagated by Monte Carlo simulations of firn models generated from the parameter distributions of snow density, 2015 − 2017 SMB, and MERRA temperature. We applied ±31 days uncertainty to the measured ages of isochrones within the simulations.

5. DISCUSSION

We developed our analysis within the interior region of Greenland where there was significant spatial variation in accumulation, but little melt, to develop confidence in this type of radar retrieval for density and SMB. The MxHL SMB has four sources of uncertainty (depth, density, temperature, and age) which were independently assessed and then propagated through the MxHL model by Monte Carlo simulation to estimate the SMB mean and standard deviation for each year of $1984 - 2017$. On average, the difference between GTC15 and MxHL SMB is small enough to accept the MxHL measured-modeled densities in place of extrapolating the measured firn core density along GTC15 Spur West. Extrapolated densities are likely to be much less accurate farther from core sites and in the percolation zone, due to increased near-surface pore space reduction caused by melt water infiltration (Harper and others, 2012). We also expect the accuracy of the HL density model to break down at elevations within the percolation zone (Brown and others, 2012). Annual fluctuations in density, and density excursions due to warming events, are not captured in the HL model. Using the MxRadar, we have the ability to measure the density profile in the percolation zone with additional layer picking for near-surface velocity analysis, but the NMO approach is sensitive only to the average density of intervals in between the layer picks (Dix, 1955) and is susceptible to errors due to subsurface velocity heterogeneities and data noise (Al-Chalabi, 1974).

In the upper $\sim 2\ m$ of the firn column we replaced modeled densities with a linear fit between the two radar measurements of snow and firn density using the surface wave and the reflection from the fall 2014 IRH. This reduced the near-surface bias present in the HL density profile and we found strong correlation between the densities of these independent radar measurements. The richness of the MxRadar data stream permits geostatistical analysis at the sub-kilometer scale. Our findings indicate that local (on the order of $1\ km$ neighborhood) processes control the GrIS dry snow density. The similarity in spatial patterns of radar estimated surface snow density, up to $\sim 2\ km$ lag distance, contrasts the findings that no correlation exists between surface snow density, latitude, longitude, or elevation (Fausto and others, 2018), which is likely due to the limited observations of snow density at the $< 1\ km$ and $< 10\ km$ scales within the *Surface Mass Balance and Snow Depth on Sea Ice Working Group* dataset (Montgomery and others, 2018). Our variogram analysis was tested to $15\ km$ lag separations along three azimuths; this indicates directionality in the spatial pattern of density, likely due to wind. Future application of this method to the $4000+\ km$ traverse will allow exploration of variations at much larger scales.

The 2014 – 2017 SMB appears to be overestimated by MxHL, though the near-surface radar velocity analysis was focused on this range. We support the radar findings here with the understanding that firn samples recovered from these depths are susceptible to *in situ* losses due to their unconsolidated nature. The radar retrieval has a sample footprint of approximately $\sim 25\ m$ (twice the length of the antenna array) and is nondestructive, while the borehole diameter is $\sim 8cm$ and samples only one point in space. It is also likely that the age model is less accurate nearest the ice sheet surface due to core sample loss; however, we sacrifice greater accuracy in the radar domain because of the limitations in our ability to interpret depth image. The fall 2014 horizon was the latest IRH measured in our analysis. Picking annual reflection horizons later than 2014, near the model boundary, created steep gradients in the numerical derivative required to estimate the SMB which yielded erroneous values.

We see evidence of the 2012 melt event (Nghiem and others, 2012) in the filtered depth image (Fig. 8). At three meters depth, the top of the reflection sequence represents January 2013, and at four meters depth, the bottom of the sequence is January 2011. This IRH sequence expresses fading and discontinuity that, we hypothesize, is the result of 2012 melt water infiltration. Measured at GTC15, the 2011 annual layer has a melt feature percentage of 7.9%. However, melt water induced firn densification does not explain the inaccuracy in 2010 MxHL SMB, as 2010 recorded 0% melt feature percentage at GTC15. The MxHL density model is accurate within the 2010 annual layer, rather our estimate of the 2010 annual layer thickness is 22 cm thinner than measured at GTC15. This is the second largest error in annual layer thickness, only behind the 2015 layer which was estimated to be 24 cm thicker than measured at GTC15 because of the aforementioned issues in estimating SMB near the model boundary. The degraded image quality of the 2011 – 2013 IRH sequence inhibited our ability to interpret the age sequence accurately enough to define the annual layer thicknesses for 2011 and 2012. Instead, we relied on interpolation to approximate the thickness of these horizons. The leading source of error in the historical SMB reconstruction are inaccuracies in the age model that result from our ability to interpret the radar image.

The multidecadal average SMB for the period 1984 – 2017 at GTC15 has remained nearly constant. Yet, sinusoidal variability in SMB on the decadal time scale is apparent in the MxHL historical SMB reconstruction and is confirmed by GTC15 SMB. Decadal variability in the MxHL reconstruction would not be observable without the application of structure-oriented filtering and interpretation that permitted an accurate instantaneous SMB model. For GPR imagery expressing small or gradual SMB variability it may be sufficient to apply the structure-oriented filter in the Wheeler domain without the steps of interpretation, age model corrections, and image re-flattening (Section S.1.6). The snow density estimation component is unique to the multi-offset radar and integral in our ability to parameterize the HL model. However, the structure-oriented filtering can be applied to any GPR imagery of isochronous firn, provided a stratigraphic age model in the radar travel-time domain that is used as a proxy for the firn structure.

Along GTC15 Spur West, we expect the largest errors due to firn advection to occur across the studied undulations (Fig. 7 and Fig. 8), where the SMB gradient is largest and oscillating. The two undulations here represent the same feature observed on outbound and inbound traverses, and serve as a demonstration of the repeatability of the methods. In regions where the spatial gradient in SMB is dynamic or ice sheet surface velocities are large, the advection of firn mass decreases the accuracy of radar estimated SMB. On Pine Island Glacier, with ice surface velocities on the order of $10 - 10^3$ m a^{-1}, strain corrections applied to the accumulation model amounted to a 1% correction to the $1986 - 2014$ average SMB (Konrad and others, 2019). Ice surface velocities along GTC15 Spur West are on the order of 10 m a^{-1} (Joughin and others, 2018), and therefore we accept a contribution of error that is an order of magnitude less than the uncertainty, by not applying corrections for the SMB due to advection.

It would be advantageous to model the firn age-structure using the kinematic wave equation (Ng and King, 2011) to capture the advection process imprinted on the radiostratigraphy without having to interpret the Wheeler domain radargram. We picked horizons in the Wheeler domain as a necessary step in applying the structure-oriented filter to the GTC15 Spur West radargram. This interpretive process could be avoided by generating the relative age using the kinematic wave equation. Yet, this model requires an independent estimate of firn density and accumulation to satify the initial and boundary conditions. Deep learning techniques have been recently applied to seismic imaging that automate structure-oriented filtering and horizon interpretation problems. By generating synthetic seismograms from numerical structural models as training data (Wu and others, 2020), relative stratigraphic age models have been recovered from real seismic data and used for automated isochrone horizon interpretation (Geng and others, 2020). The kinematic wave model could serve as a basis for generating synthetic radargrams to be used in a deep learning application.

6. CONCLUSIONS

GreenTrACS conducted the first multi-offset GPR traverse on the Greenland Ice Sheet, covering a total distance of 4436 km. We examined a 78 km section of the GreenTrACS 2017 traverse (GTC15 Spur West) to develop the methodology for multi-offset GPR wave velocity, imaging, and uncertainty analyses to accurately quantify the surface snow density, average snow density, firn density, instantaneous SMB, annual SMB, and multidecadal average SMB for the period 1984 − 2017. Using travel-time inversion of the radar waveforms, we continuously mapped Greenland snow density without manual observations of the snow. We found consistent spatial correlation of near-surface density for separations up to 2 km distance and significant correlation ($\mathrm{R}^2 = 0.67$, $p = 0$) between near-surface snow density and average snow density of the upper 2 m. We demonstrated the use of the Herron and Langway (1980) model that was parameterized by the radar-derived snow density, radar-derived SMB (2015 − 2017), and MERRA 2 m air temperature, to estimate firn density and age. Our measured-modeled firn density in the dry snow accumulation zone accurately represents the firn core but can be performed continuously along a traverse in the field without destructive measurements.

GreenTrACS Core 15 Spur West presented an interesting challenge because of spatial SMB variability that is enhanced by the surface topography. In the dry snow zone, topographic lows tend to accumulate greater amounts of snow. This effect induces undulations in the firn stratigraphy which steepen with depth, due to the persistence of increased accumulation. Folds in the firn stratigraphy are difficult to image clearly with conventional GPR processing methods. Borrowing from seismic interpretation methods, we facilitated structure-oriented filtering by utilizing the firn age model to determine the firn structure. In doing so, we furthered the application of the IRH theory, which is integral in SMB analyses conducted with radar imagery. This innovation enabled our interpretation of deeper (from 16.60 ± 0.04 m to 20.15 ± 0.04 m at GTC15) and older (from 1991 ± 31 days to 1984 ± 31 days) layers and permitted tuning the age model to a degree of accuracy which allowed us to derive instantaneous estimates of SMB which we averaged annually and multidecadally. Future work will include application of this methodology to the entire $4000+$ km GreenTrACS traverse, with independent evaluation at the 16 core sites.

SUPPLEMENTARY MATERIAL

The supplemental material for this article can be found at

ACKNOWLEDGEMENTS

Greenland Traverse for Accumulation and Climate Studies was funded by the National Science Foundation Office of Polar Programs: Awards # 1417921 and # 1417678. Additional support of this work was awarded through the NASA Idaho Space Grant Consortium Graduate Fellowship and the STEM Student Employment Program through the U.S. Army Engineer Research and Development Center, Cold Regions Research and Engineering Laboratory.

The author's would like to thank Dr. Steve Arcone and an anonymous reviewer for their recommendations which improved the communication of technical aspects of this work and Journal of Glaciology Scientific Editor Dr. Shad O'Neel for his additional review of our manuscript which greatly improved its readability.

DATA AVAILABILITY

The 2017 GreenTrACS multi-channel GPR data can be found at https://doi.org/10.18739/A21G0HT84. The MATLAB scripts used in this analysis are continually under development and can be forked from the github repository https://github.com/tatemeehan/GreenTrACS_MxRadar.

REFERENCES

Al-Chalabi M (1974) An Analysis of Stacking, RMS, Average, and Interval Velocities Over a Horizontally Layered Ground. *Geophys. Prospect.*, **22**, 458–475 (doi: 10.1111/j.1365-2478.1974.tb00099.x)

Barrett BE, Murray T and Clark R (2007) Errors in Radar CMP Velocity Estimates Due to Survey Geometry, and Their Implication for Ice Water Content Estimation. *J. Environ. Eng. Geophys.*, **12**(1), 101–111, ISSN 1083-1363 (doi: 10.2113/JEEG12.1.101)

Bradford JH, Nichols J, Mikesell TD and Harper JT (2009) Continuous profiles of electromagnetic wave velocity and water content in glaciers: an example from Bench Glacier, Alaska, USA. *Ann. Glaciol.*, **50**(51), 1–9, ISSN 0260-3055 (doi: 10.3189/172756409789097540)

Brown J, Harper J, Pfeffer WT, Humphrey N and Bradford J (2011) High-resolution study of layering within the percolation and soaked facies of the Greenland ice sheet. *Ann. Glaciol.*, **52**(59), 35–42, ISSN 02603055 (doi: 10.3189/172756411799096286)

Brown J, Bradford J, Harper J, Pfeffer WT, Humphrey N and Mosley-Thompson E (2012) Georadar-derived estimates of firn density in the percolation zone, western Greenland ice sheet. *J. Geophys. Res. Earth Surf.*, **117**(1), 1–15, ISSN 21699011 (doi: 10.1029/2011JF002089)

Brown J, Harper J and Humphrey N (2017) Liquid water content in ice estimated through a full-depth ground radar profile and borehole measurements in western Greenland. *Cryosph.*, **11**(1), 669–679, ISSN 19940424 (doi: 10.5194/tc-11-669-2017)

Dix CH (1955) Seismic velocities from surface measurements. *Geophysics*, **20**(1), 68–86, ISSN 1070485X (doi: 10.1190/1.1438126 v. 20 no. 1 p. 68-86)

Eisen O, Nixdorf U, Wilhelms F and Miller H (2002) Electromagnetic wave speed in polar ice: Validation of the common-midpoint technique with high-resolution dielectric-profiling and density measurements. *Ann. Glaciol.*, **34**, 150–156, ISSN 02603055 (doi: 10.3189/172756402781817509)

Fausto RS, Box JE, Vandecrux B, van As D, Steffen K, MacFerrin MJ, Machguth H, Colgan W, Koenig LS, McGrath D, Charalampidis C and Braithwaite RJ (2018) A Snow Density Dataset for Improving Surface Boundary Conditions in Greenland Ice Sheet Firn Modeling. *Front. Earth Sci.*, **6**(May), 1–10 (doi: 10.3389/feart.2018.00051)

Fettweis X, Box JE, Agosta C, Amory C, Kittel C, Lang C, Van As D, Machguth H and Gallée H (2017) Reconstructions of the 1900-2015 Greenland ice sheet surface mass balance using the regional climate MAR model. *Cryosphere*, **11**(2), 1015–1033, ISSN 19940424 (doi: 10.5194/tc-11-1015-2017)

Geng Z, Wu X, Shi Y and Fomel S (2020) Deep learning for relative geologic time and seismic horizons. *Geophysics*, **85**(4), 1–47, ISSN 0016-8033 (doi: 10.1190/geo2019-0252.1)

Graeter KA, Osterberg EC, Ferris DG, Hawley RL, Marshall HP, Lewis G, Meehan T, McCarthy F, Overly T and Birkel SD (2018) Ice Core Records of West Greenland Melt and Climate Forcing. *Geophys. Res. Lett.*, **45**(7), 3164–3172, ISSN 19448007 (doi: 10.1002/2017GL076641)

Grima C, Blankenship DD, Young DA and Schroeder DM (2014) Surface slope control on firn density at Thwaites Glacier, West Antarctica: Results from airborne radar sounding. *Geophys. Res. Lett.*, **41**(19), 6787–6794 (doi: 10.1002/2014GL061635)

Harper J, Humphrey N, Pfeffer WT, Brown J and Fettweis X (2012) Greenland ice-sheet contribution to sea-level rise buffered by meltwater storage in firn. *Nature*, **491**(7423), 240–243, ISSN 0028-0836 (doi: 10.1038/nature11566)

Hawley RL, Courville ZR, Kehrl LM, Lutz ER, Osterberg EC, Overly TB and Wong GJ (2014) Recent accumulation variability in northwest Greenland from ground-penetrating radar and shallow cores along the Greenland Inland Traverse. *J. Glaciol.*, **60**(220), 375–382, ISSN 00221430 (doi: 10.3189/2014JoG13J141)

Herron MM and Langway CC (1980) Firn Densification: An Emperical Model. *J. Glaciol.*, **25**(93), 373–385, ISSN 00221430

Joughin I, Smith BE and Howat IM (2018) A complete map of Greenland ice velocity derived from satellite data collected over 20 years. *J. Glaciol.*, **64**(243), 1–11, ISSN 0022-1430 (doi: 10.1017/jog.2017.73)

Konrad H, Hogg AE, Mulvaney R, Arthern R, Tuckwell RJ, Medley B and Shepherd A (2019) Observations of surface mass balance on Pine Island Glacier, West Antarctica, and the effect of strain history in fast-flowing sections. *J. Glaciol.*, 1–10, ISSN 0022-1430 (doi: 10.1017/jog.2019.36)

Lenaerts JT, Medley B, van den Broeke MR and Wouters B (2019) Observing and Modeling Ice Sheet Surface Mass Balance. *Rev. Geophys.*, ISSN 19449208 (doi: 10.1029/2018RG000622)

Lewis G, Osterberg E, Hawley R, Marshall HP, Meehan T, Graeter K, McCarthy F, Overly T, Thundercloud Z and Ferris D (2019) Recent precipitation decrease across the western Greenland ice sheet percolation zone. *Cryosph.*, **13**(11), 2797–2815, ISSN 1994-0424 (doi: 10.5194/tc-13-2797-2019)

Loewe F (1970) Screen Temperatures and 10m Temperatures. *J. Glaciol.*, **9**(56), 263–268, ISSN 0022-1430 (doi: 10.3189/S0022143000023571)

Looyenga H (1965) Dielectric constants of heterogeneous mixtures. *Physica*, **31**(3), 401–406, ISSN 0031-8914 (doi: https://doi.org/10.1016/0031-8914(65)90045-5)

Matheron G (1963) Principles of geostatistics. *Econ. Geol.*, **58**(8), 1246–1266, ISSN 1554-0774 (doi: 10.2113/gsecongeo.58.8.1246)

Meyer CR, Keegan KM, Baker I and Hawley RL (2020) A model for French-press experiments of dry snow compaction. *Cryosph.*, **14**(5), 1449–1458, ISSN 1994-0424 (doi: 10.5194/tc-14-1449-2020)

Montgomery L, Koenig L and Alexander P (2018) The SUMup dataset: Compiled measurements of surface mass balance components over ice sheets and sea ice with analysis over Greenland. *Earth Syst. Sci. Data*, **10**(4), 1959–1985, ISSN 18663516 (doi: 10.5194/essd-10-1959-2018)

Morlighem M (2017) Icebridge bedmachine greenland, version 3 (doi: 10.5067/2CIX82HUV88Y)

Navarro F and Eisen O (2009) Ground-penetrating radar in glaciological applications. In P Pellikka and GW Rees (eds.), *Remote Sens. Glaciers*, December, chapter 11, 195–229 (doi: 10.1201/b10155-12)

Ng F and King EC (2011) Kinematic waves in polar firn stratigraphy. *J. Glaciol.*, **57**(206), 1119–1134, ISSN 0022-1430 (doi: 10.3189/002214311798843340)

Nghiem SV, Hall DK, Mote TL, Tedesco M, Albert MR, Keegan K, Shuman CA, DiGirolamo NE and Neumann G (2012) The extreme melt across the Greenland ice sheet in 2012. *Geophys. Res. Lett.*, **39**(20), 6–11, ISSN 00948276 (doi: 10.1029/2012GL053611)

Noël B, Jan Van De Berg W, MacHguth H, Lhermitte S, Howat I, Fettweis X and Van Den Broeke MR (2016) A daily, 1 km resolution data set of downscaled Greenland ice sheet surface mass balance (1958-2015). *Cryosphere*, **10**(5), 2361–2377, ISSN 19940424 (doi: 10.5194/tc-10-2361-2016)

Overly TB, Hawley RL, Helm V, Morris EM and Chaudhary RN (2016) Greenland annual accumulation along the EGIG line, 1959-2004, from ASIRAS airborne radar and neutron-probe density measurements. *Cryosphere*, **10**(4), 1679–1694, ISSN 19940424 (doi: 10.5194/tc-10-1679-2016)

Pearson K (1907) *On further methods of determining correlation*, volume 16. Dulau and Company

Porter C, Morin P, Howat I, Noh MJ, Bates B, Peterman K, Keesey S, Schlenk M, Gardiner J, Tomko K, Willis M, Kelleher C, Cloutier M, Husby E, Foga S, Nakamura H, Platson M, Wethington J Michael, Williamson C, Bauer G, Enos J, Arnold G, Kramer W, Becker P, Doshi A, D'Souza C, Cummens P, Laurier F and Bojesen M (2018) ArcticDEM (doi: 10.7910/DVN/OHHUKH)

Shepherd A, Ivins E, Rignot E, Smith B, van den Broeke M, Velicogna I, Whitehouse P, Briggs K, Joughin I, Krinner G, Nowicki S, Payne T, Scambos T, Schlegel N, A G, Agosta C, Ahlstrøm A, Babonis G, Barletta VR, Bjørk AA, Blazquez A, Bonin J, Colgan W, Csatho B, Cullather R, Engdahl ME, Felikson D, Fettweis X, Forsberg R, Hogg AE, Gallee H, Gardner A, Gilbert L, Gourmelen N, Groh A, Gunter B, Hanna E, Harig C, Helm V, Horvath A, Horwath M, Khan S, Kjeldsen KK, Konrad H, Langen PL, Lecavalier B, Loomis B, Luthcke S, McMillan M, Melini D, Mernild S, Mohajerani Y, Moore P, Mottram R, Mouginot J, Moyano G, Muir A, Nagler T, Nield G, Nilsson J, Noël B, Otosaka I, Pattle ME, Peltier WR, Pie N, Rietbroek R, Rott H, Sandberg Sørensen L, Sasgen I, Save H, Scheuchl B, Schrama E, Schröder L, Seo KW, Simonsen SB, Slater T, Spada G, Sutterley T, Talpe M, Tarasov L, van de Berg WJ, van der Wal W, van Wessem M, Vishwakarma BD, Wiese D, Wilton D, Wagner T, Wouters B, Wuite J and Team TI (2020) Mass balance of the Greenland Ice Sheet from 1992 to 2018. *Nature*, **579**(7798), 233–239, ISSN 1476-4687 (doi: 10.1038/s41586-019-1855-2)

Spikes VB, Hamilton GS, Arcone SA, Kaspari S and Mayewski PA (2004) Variability in accumulation rates from GPR profiling on the West Antarctic plateau. *Ann. Glaciol.*, **39**, 238–244, ISSN 02603055 (doi: 10.3189/172756404781814393)

van Kampenhout L, Lenaerts JTM, Lipscomb WH, Sacks WJ, Lawrence DM, Slater AG and van den Broeke MR (2017) Improving the Representation of Polar Snow and Firn in the Community Earth System Model. *J. Adv. Model. Earth Syst.*, **9**(7), 2583–2600, ISSN 19422466 (doi: 10.1002/2017MS000988)

Vandecrux B, Fausto RS, Langen PL, van As D, MacFerrin M, Colgan WT, Ingeman-Nielsen T, Steffen K, Jensen NS, Møller MT and Box JE (2018) Drivers of Firn Density on the Greenland Ice Sheet Revealed by Weather Station Observations and Modeling. *J. Geophys. Res. Earth Surf.*, **123**(10), 2563–2576, ISSN 21699011 (doi: 10.1029/2017JF004597)

Vaughan DG, Corr HFJ, Doake CSM and Waddington ED (1999) Distortion of isochronous layers in ice revealed by ground-penetrating radar. *Nature*, **398**(6725), 323–326, ISSN 0028-0836 (doi: 10.1038/18653)

Wharton RP, Hazen GA, Rau RN and Best DL (1980) Advancements In Electromagnetic Propagation Logging. In *SPE Rocky Mt. Reg. Meet.*, Society of Petroleum Engineers, Society of Petroleum Engineers (doi: 10.2118/9041-MS)

Wheeler HE (1958) Time-Stratigraphy. *Am. Assoc. Pet. Geol. Bull.*, **42**(5), 1047–1063, ISSN 0149-1423 (doi: 10.1306/0BDA5AF2-16BD-11D7-8645000102C1865D)

Wu X, Geng Z, Shi Y, Pham N, Fomel S and Caumon G (2020) Building realistic structure models to train convolutional neural networks for seismic structural interpretation. *GEOPHYSICS*, **85**(4), WA27–WA39, ISSN 0016-8033 (doi: 10.1190/geo2019-0375.1)

Zwally HJ and Li J (2002) Seasonal and interannual variations of firn densification and ice-sheet surface elevation at the Greenland summit. *J. Glaciol.*, **48**(161), 199–207, ISSN 00221430 (doi: 10.3189/172756502781831403)

List of Figures

List of Tables

Historical surface mass balance reconstruction 1984 – 2017 from GreenTrACS multi-offset ground-penetrating radar

Tate G. MEEHAN,[1,2] H.P. MARSHALL,[1,2] John H. BRADFORD,[3] Robert L. HAWLEY,[4] Thomas B. OVERLY,[5,6] Gabriel LEWIS,[4] Karina GRAETER,[4] Erich OSTERBERG,[4] Forrest McCARTHY [4]

[1]*Department of Geoscience, Boise State University, Boise, ID, USA*

[2] *U.S. Army Cold Regions Research and Engineering and Laboratory, Hanover, NH, USA*

[3]*Department of Geophysics, Colorado School of Mines, Golden, CO, USA*

[4]*Department of Earth Sciences, Dartmouth College, Hanover, NH, USA*

[5]*Cryospheric Sciences Lab, NASA Goddard Space Flight Center, Greenbelt, MD, USA*

[6]*Earth System Science Interdisciplinary Center, University of Maryland, College Park, MD, USA*

Correspondence: Tate Meehan <tatemeehan@u.boisestate.edu>

S.1. SUPPLEMENTARY MATERIAL

We introduced the methodological concepts of our radar measured and modeled approach for reconstructing historical SMB in Section 3. Within supplement S.1, we provide the core computations used and give more insight into the methods of velocity analysis, parameter estimation, imaging, and interpretation. The flow diagram (Fig. S.1) works through the MxHL process to show not only the radar processing steps, but also the interconnectivity between the radar measured information and the HL firn model.

We introduce our methods for interpreting the radar imagery (Section S.1.1) and conducting horizon velocity analysis (Section S.1.2). We use the radar wave velocity information for snow parameter estimation (see sections S.1.3 and S.1.4), and use these results to parameterize the MxHL model in Section S.1.5. We then extend the capabilities of the firn age and density models to enable our structure-oriented filter (see section S.1.6) and refine our estimate of SMB using relative age model updates in the stratigraphic age domain (Wheeler, 1958) and absolute age model updates in the depth domain (see section S.1.7).

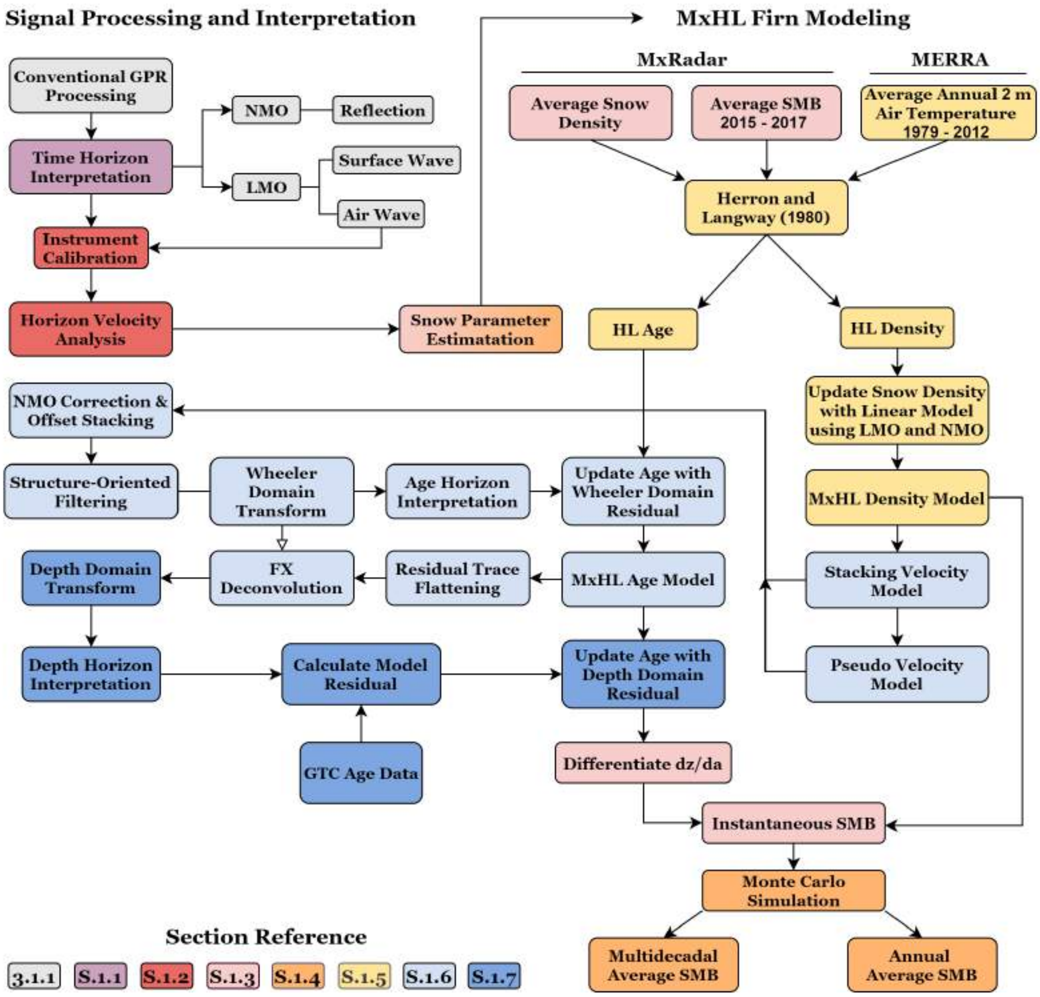

Fig. S.1: The workflow for our measured-modeled historical SMB reconstruction. Colors correspond to the section reference where the concept is detailed. For example, the gradient colors of *Snow Parameter Estimation* indicate that concept spans sections S.1.3 and S.1.4.

S.1.1. Travel-time Horizon Interpretation

We developed a phase and amplitude tracking, semi-automatic picking algorithm to measure the travel-times of radar wavefield events. The picker is semi-automatic in that an initial pick on the horizon seeds the automatic tracking. Similar to picking algorithms described by Dorn (1998), our seeded picker transforms a window of the radargram surrounding the horizon of interest into radial distance and dip angle coordinates (r, θ) and stacks the windowed image along the θ direction. The algorithm determines the optimal direction by maximizing stacked amplitude. The subsequent automatic pick is predicted 5 traces ahead, which is approximately the length of the radar array, along the linear path of maximum stack. Then the windowed polar transformation and prediction is repeated automatically. Travel-time picks between predictions are interpolated using a distance-weighted scheme. The program has the capability to toggle manual selection or re-seed the pick if the algorithm goes awry. We picked the direct air wave, the direct surface wave, and the reflected wave from the fall 2014 layer on each of the nine radargrams for velocity analysis. These early-time events exhibit low noise with a travel-time standard deviation of 0.2 ns (1 sample). Using this layer picker, we also picked five age-horizons (see section S.1.6) and 16 depth-horizons (see section S.1.7) to update the age model for SMB calculation.

S.1.2. Horizon Velocity Analysis

Direct (air-coupled and surface-coupled) waves obey the linear travel-time equation known as linear moveout (LMO)

$$t = t_0 + \frac{x}{V_{LMO}} \quad , \tag{S.1}$$

where t is the measured one-way travel time and x is the antenna offset, with intercept time (t_0) and velocity (V_{LMO}) representing unknown parameters. Reflected radar waves exhibit non-linear travel-times as a function of offset that are approximated by NMO. The $x^2 - t^2$ method (Green, 1938) linearizes the NMO equation

$$t^2 = t_0^2 + \frac{x^2}{V_{NMO}^2} \quad . \tag{S.2}$$

where t is now the measured two-way travel time and V_{NMO} is the NMO velocity or *stacking velocity.*

Prior to velocity analysis of the surface wave and reflection, we calibrated the timing of each radar channel. Channel consistent travel-time overheads are caused within the Sensors & Software multi-channel adapter by variations in the path lengths of the circuitry and cables. During the instrument calibration process we apply corrections (on the order of nanoseconds) to the time sampling of each channel by picking the air-wave arrival times (Fig. 4) and solving Eq. (S.1) for the set of perturbations that let $t_0 = 0$ and $V_{LMO} = 0.2998\ m/ns$, the velocity of EM waves in free-space.

We applied linear regression for near-surface velocity analyses using the picked, one-way travel-times of direct wave arrivals traveling laterally through the shallow snow and the two-way travel-times of reflected arrivals from the fall 2014 horizon. To cast each system of equations into a matrix-vector product, the velocity parameter is linearized by its reciprocal, called slowness, as $S = \frac{1}{V}$. The linear system of equations has the form $\mathbf{Gm} = \mathbf{d}$ for the vector $\mathbf{d}$ containing the recorded travel-times for the respective moveout events. Equations (S.3) and (S.4) are the monomial basis functions used for linear regression of LMO and NMO events. Equations (S.5) and (S.6) are the model parameters and equations (S.7) and (S.8) are the respective data. The least squares solution for $\mathbf{m} = \mathrm{G}^{-1}\mathbf{d}$ is optionally solved in either L_2 or L_1 norm. We used the L_2 solution which was estimated by QR factorization (Businger and Golub, 1965). Advantages and convergence criteria of the L_1 solution are discussed in Aster and others (2019).

$$\mathrm{G}_{\mathrm{LMO}} = \begin{bmatrix} 1 & x_1 \\ \vdots & \vdots \\ 1 & x_m \end{bmatrix} \quad (\mathrm{S}.3) \qquad \mathbf{m}_{\mathrm{LMO}} = \begin{bmatrix} t_0 \\ \\ S_{LMO} \end{bmatrix} \quad (\mathrm{S}.5) \qquad \mathbf{d}_{\mathrm{LMO}} = \begin{bmatrix} t_1 \\ \vdots \\ t_m \end{bmatrix} \quad (\mathrm{S}.7)$$

$$\mathrm{G}_{\mathrm{NMO}} = \begin{bmatrix} 1 & x_1^2 \\ \vdots & \vdots \\ 1 & x_m^2 \end{bmatrix} \quad (\mathrm{S}.4) \qquad \mathbf{m}_{\mathrm{NMO}} = \begin{bmatrix} t_0^2 \\ \\ S_{NMO}^2 \end{bmatrix} \quad (\mathrm{S}.6) \qquad \mathbf{d}_{\mathrm{NMO}} = \begin{bmatrix} t_1^2 \\ \vdots \\ t_m^2 \end{bmatrix} \quad (\mathrm{S}.8)$$

S.1.3. Parameter Estimation: Depth, Density, and SMB

The wave propagating along the ice sheet surface is estimated to respond to snow depths no greater than the wavelength

$$z_{LMO} = \frac{V_{LMO}}{f} \quad , \tag{S.9}$$

calculated from the nominal radar frequency ($f \approx 500\ MHz$) and snow velocity (V_{LMO}). Eq. (S.9) was developed on Occam's razor. This simple approximation for the penetration of the surface coupled wave was found to be consistent with the depth and average density measured at GTC15 and Pit 15 W. The depth of the reflection horizon for a subsurface propagating wave

$$z_{NMO} = \frac{V_{NMO} \cdot t_0}{2} \quad , \tag{S.10}$$

is estimated assuming that the NMO approximation is valid, meaning that V_{NMO} is approximately equal to the average velocity above the horizon.

The complex refractive index method (CRIM) equation relates a mixture of known dielectric properties to an estimated effective bulk property (Wharton and others, 1980). We estimated the average snow density from the EM velocity by the CRIM equation

$$\rho_s = \rho_i \left(1 - \frac{V_a(V_i - V_s)}{V_s(V_i - V_a)}\right) \quad , \tag{S.11}$$

letting the snow and firn pore space be unoccupied free space with the velocity $V_a = 0.2998\ m/ns$ and the matrix to be composed of only ice with EM velocity $V_i = 0.1689\ m/ns$, and density $\rho_i = 917\ kg/m^3$ (Ulaby and others, 1986). The quantities are given the subscript a for air, i for ice, or s for snow and firn. Liquid water within the firn layer was neither present within snow pits nor firn cores sampled during this field study, and is therefore not considered in Eq. (S.11).

Surface mass balance is conventionally measured using GPR by interpreting a select few IRHs using a constant age interval and applying the average normalized snow and firn density over this interval (e.g. Lewis and others, 2019). Instead, we rely on the models of density and age, which are discretized in depth at a comparable resolution to the GPR data. We measured instantaneous SMB ($\dot{b}$), in meters of water equivalent per an infinitesimal time

$$\dot{b} = \frac{\rho_s}{\rho_w}\frac{\mathrm{d}z}{\mathrm{d}a} \quad , \tag{S.12}$$

as the product of the snow and firn density, normalized by the density of water (ρ_w), and the submergence rate of stratigraphic isochrones $\left(\frac{\mathrm{d}z}{\mathrm{d}a}\right)$ in a Lagrangian reference frame. The submergence rate is the continuous equivalent of interpreting a few horizons with large age intervals. In practice, we approximated this derivative using second-order accurate finite difference weights calculated from the Fornberg (1988) algorithm, because the age-depth model is not discretized in regular intervals. The median discrete interval of the age-depth model is 14 days with a minimum interval of seven days and a maximum interval of 20 days. We found that the local truncation error of the second-order accurate derivative was $5 \times 10^{-5}\ m\ w.e.\ a^{-1}$, which has a leading error term an order of magnitude less than what we consider to be significant.

S.1.4. Parameter Uncertainty: Monte Carlo Bootstrapping and Error Propagation

To ascertain the uncertainty in the radar inversion, we implemented a bootstrapping algorithm by randomly sub-sampling the CMP travel-times from the LMO and NMO horizons and re-solving the linear regression. In a roll-along fashion, travel-time observations of five neighboring CMP gathers were binned and re-sampled by removing two offsets at random and then randomly sampling one travel-time observation for each remaining offset in the bin. This algorithm creates many realizations of the intercept time and snow velocity by the jackknife technique (Efron and Stein, 1981). Realizations of depth and density were generated from the current realization of $\mathbf{m}$ following Equations (S.9) – (S.11). The bootstrapped distribution $\widehat{\mathcal{M}}$ was generated from 1000 jackknifed realizations to establish uncertainty regions (Efron and Tibshirani, 1986). A distribution was gathered for each parameter: intercept travel-time, velocity, depth, and density. The mean of $\widehat{\mathcal{M}}$ yields the expected value of the parameter ($\widehat{m}$) with a standard deviation ($\widehat{\sigma}$). We developed uncertainty regions for each bootstrapped distribution assuming the standard normal distribution

$$\widehat{m} \pm \widehat{z}\, \widehat{\sigma} \quad , \tag{S.13}$$

and assessed the z-score at $\widehat{z} = 1$, which has the central interval of $1\widehat{\sigma}$ (Efron and Tibshirani, 1986). The jackknifed estimates of variance for snow density and depth provide the means to estimate uncertainty in the $2015 - 2017$ SMB. We estimated the variance of SMB by the linear error propagation equation

$$\widehat{\sigma}_{\dot{b}}^2 = \widehat{\sigma}_z^2 \rho^2 + \widehat{\sigma}_\rho^2 z^2 + 2\widehat{\sigma}_{\rho z} \rho z \quad , \tag{S.14}$$

where the covariance $\widehat{\sigma}_{\rho z}$ was calculated from the parameter distributions. The resulting uncertainty measure is the standard interval developed from Eq. (S.13). The snow parameters and uncertainties presented in Fig. 5 were smoothed using a Gaussian kernal with a standard deviation of 250 m.

As we presented in Fig. 9, we propagated uncertainties in SMB by Monte Carlo simulation, which incorporated the uncertainty in the age of dated isochrones ($\sigma_a = \pm 31$ days) and the uncertainties in the snow parameters used to generate the firn model (Section S.1.5). We estimated the ± 31 day uncertainty by summing in quadrature the uncertainties in the firn core age (± 18 days; Rupper and others (2015)) and the radar estimated depth that was mapped to the GTC15 age-depth scale (± 25 days) developed by Lewis and others (2019). We delimited the annual SMB calculation between January 1, 1984 and January 1, 2017, which are the complete years between the date of the earliest layer picked and the date of data acquisition. We filtered the outlying 1% of the instantaneous SMB model and interpolated between neighboring values. We quantified annual average SMB and its uncertainty using Monte Carlo simulation, by generating 1000 randomly initialized density-depth models (Section S.1.5) from the snow parameter distributions. Rather than randomly generating an age model in this process, because we updated the age-depth model by interpreting IRHs (Section S.1.6), we interpolated the age model to the depth axis that was defined by the Monte Carlo realization of the density model. We calculated the numerical derivative to estimate the instantaneous SMB (Eq. (S.12)), extracted the intervals that composed each annual layer, and averaged the samples of instantaneous SMB into one realization of annual SMB. After 1000 realizations were generated for each of 33 years in the period $1984-2017$, we calculated the multidecadal mean SMB and variance using Monte Carlo resampling. Repeating for 1000 simulations, we randomly sampled an annual SMB realization from 10 annual intervals and averaged. In the following section, to clarify the capabilities of the radar analysis we ignore the uncertainties in the firn core ages and demonstrate the radar inversion as the only source of uncertainty in SMB when paramertizing the MxHL model.

S.1.5. Parameterizing the MxRadar - Herron and Langway (1980) Model

The Herron and Langway (1980, HL) model requires three parameters: mean snow density, mean annual accumulation, and 10 m firn temperature. We use the snow properties estimated by the radar inversion (Fig. 5) and MERRA reanalysis temperature to parameterize the HL model in our measured-modeled, MxRadar-HL, framework. We chose the density parameter as the average of the densities estimated by the surface-wave (LMO) analysis and the reflected wave (NMO) analysis of the fall 2014 isochronous reflection horizon (IRH). We approximated the accumulation parameter using the radar estimated SMB (Eq. (S.12)) that represented the average of the previous ~ 2.5 years – as the IRH depth indicates the date November 30, 2014, established by the firn core analysis, and the date of acquisition was June 13, 2017. Mean annual 2 m air temperature was calculated from MERRA ($1979-2012$) data (Birkel, 2018) and used as a proxy for 10 m firn temperature (Loewe, 1970). MERRA annual temperatures at GTC15 over the period $1979-2012$ show an increase of $0.06 \pm 0.01\ ^{\circ}C\ a^{-1}$ with a mean of $-25.7 \pm 1.0\ ^{\circ}C$.

We evaluated the MxHL parameterization by comparing it to the GTC15 parametization (Fig. S.2) and an optimum set of parameters that were determined by minimizing

$$\phi = \frac{\mathrm{RMS}(\mathcal{T}_{HL} - \mathcal{T}_{GTC15})}{\mathrm{range}(\mathcal{T}_{GTC15})} + \frac{\mathrm{RMS}(\rho_{HL} - \rho_{GTC15})}{\mathrm{range}(\rho_{GTC15})} \quad , \tag{S.15}$$

using the Nelder and Mead (1965) method (NM) for nonlinear optimization. The objective function ϕ (Eq. (S.15)) measures the root-mean-squared error of the modeled (HL) and measured (GTC15) age ($\mathcal{T}$) and density (ρ) as a percentage, normalized by the range in the data for the entire depth of GTC15 ($\sim 28.5\ m$). An objective function measured by either $\mathcal{T}$ or ρ individually does not contain a unique global solution upon minimization. We found that an appropriate fit to GTC15 $\mathcal{T}$ or GTC15 ρ could be achieved with a range of parameterizations, alluding to the non-uniqueness which we regularized by minimizing ϕ as a function of both the age and density.

Average SMB, density, and 10 m bore hole temperature measured at GTC15 provided the true parameterization for the HL model. The age-depth scale (1969-2017) was measured by analyzing seasonal oscillations of δ^{18}O, major ions, and dust observed in the firn core (Lewis and others, 2019). Annual SMB was measured by combining the age-depth scale with the firn density (Lewis and others, 2019). We estimated the GTC15 mean annual SMB using Monte Carlo resampling to assess uncertainties (0.306 ± 0.021 m $w.e.$ a^{-1}). We chose the GTC15 density parameter (359 ± 36 kg/m^3), which is the "commonly reported average density over the first one or two meters of snow" (Herron and Langway, 1980, p. 7), at the interval that had the minimum residual with the NM optimum density. The central depth of the core interval nearest to the optimal density is 1.22 ± 0.13 m. Uncertainties in the density parameter are assumed to be within 10% of the measurement. We measured firn temperatures using borehole thermistors at 6, 8, 10, 12, and 14 m depth. After the thermistor string reached equilibrium, temperatures between 6 and 14 m depth closely agreed and we used Monte Carlo resampling to estimate the 10 m firn temperature (-24.9 ± 0.2 $°C$).

The HL model parameterized by GTC15 data yielded $\phi = 6.4\%$, which is near the optimum $\phi = 6.2\%$. The MxHL parameters obtained in the vicinity of GTC15 achieved an agreeably close fit with $\phi = 7.0\%$. Table S.1 summarizes the three HL model parameterizations and their accuracy. Figure S.2 displays the MxHL parameters overlaid on slices of Eq. (S.15) through the GTC15 parameters.

We completed the radar analyses using the MxHL model after making the following adjustments. We refined the density model using the LMO and NMO derived densities and depths to estimate the snow density-depth gradient. Using a linear model we replaced the upper one to two meters of the HL model with a piecewise segment that was extrapolated to the surface and merged with the HL model at the intersecting depth in the snow. We also refined the age model and improved the radar image quality using structure-oriented filtering (see section S.1.6).

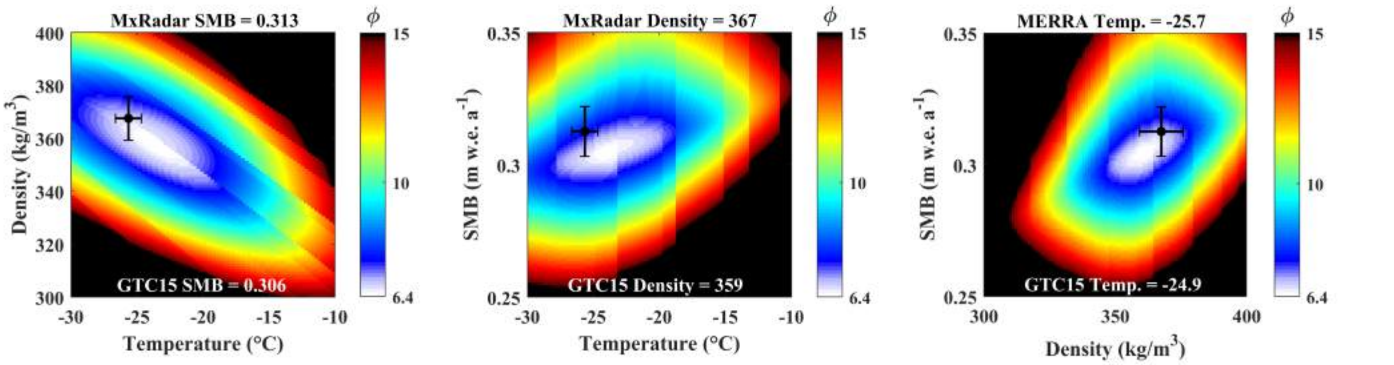

Fig. S.2: Equation S.15 is represented as slices through the GTC15 parameterization. Viewing the 3D objective function this way shows the model sensitivity to the parameters. The MxHL parameters are evaluated against the GTC15 parameterization with 1σ uncertainties. These data are summarized in Table S.1.

Table S.1: HL parameters from MxRadar (MxHL), GreenTrACS Core 15 (GTC15), and Nelder and Mead (1965) optimization (NM) are compared. Uncertainties in the GTC15 and MxHL parameterizations are expressed at 1σ. Accuracy is reported for the modeled age ($\phi_{\mathcal{T}}$) and density (ϕ_ρ) as the rms error and jointly as the normalized summed rms error ϕ.

Parameters	$\dot{\mathbf{b}}$ **(m w.e. a^{-1})**	ρ **(kg/m^3)**	**T (°C)**	$\mathcal{T}_{\mathrm{RMSE}}$ **(a)**	ρ_{RMSE} **(kg/m^3)**	ϕ **(%)**
MxHL	0.313 ± 0.009	367 ± 8	-25.7 ± 1.0	0.528	20.2	7.0
GTC15	0.306 ± 0.021	359 ± 36	-24.9 ± 0.2	0.40	20.0	6.4
NM	0.306	358	-23.1	0.350	19.0	6.2

S.1.6. Structure-oriented Filtering in the Wheeler Domain

Accumulated snow is deposited in isochronous layers that propagate slowly as the firn stratigraphy evolves and are apparent in the radiostratigraphy (Arcone and others, 2005; Ng and King, 2011). However, as demonstrated in this study, larger amplitude stratigraphic undulations with wavelengths of $\lessapprox 5$ km exhibit reduced coherence in the GPR imaging, an effect that is worsened by increased surface roughness. As described by Arcone and others (2004), artificial fading in the GPR image along the limbs of stratigraphic folds also interrupts the horizon continuity. The fading effect can be seen in Fig. 8 as a discontinuity in the inflection point of a fold at 48 km distance and ~ 11 m depth. It is important to accurately capture SMB variability at < 5 km for evaluating downscaled surface mass balance models, but as we demonstrate, this effort would be limited to only a few horizon selections here because of noise contamination in the radar section.

Structure-oriented filtering techniques often determine the structure from the time or depth image by localized eigenvalue decomposition of the image gradient tensor, such as filters applying nonlinear anisotropic diffusion (Fehmers and Höcker, 2003). We imposed the isochrone structure on the image, using the age model as a proxy for the stratigraphic structure. We flattened the firn structure by converting the time domain GPR image into coordinates of stratigraphic age, known as the Wheeler (1958) domain. We then applied linear prediction filtering, because flattening the traces improves their predictability by linear modeling. Conversion to stratigraphic coordinates can be achieved using plane wave deconstruction filters to determine local slope fields from the image (Karimi and Fomel, 2015). But it is to our advantage to work with the stratigraphic age because this information is necessary for SMB calculations. We found our approach outperformed filters that determine the structure orientation directly from the noisy image.

To implement the structure-oriented filter, we produced a noisy time domain radar section from the multi-channel imagery (Fig. 7) by first transferring the measured-modeled firn density to stacking velocity (V_{NMO}) and then applying normal moveout correction and offset stacking (Yilmaz, 2001). Provided that the radiostratigraphy in depth mimics the firn layering and is isochronous (e.g. Spikes and others, 2004), we used the HL age-depth model to estimate the firn structure orientation and age. To do so, we first converted the age model from depth to travel-time (Fig. S.3) by a vertical stretch (Margrave and Lamoureux, 2019) using the stacking velocity model. We created a pseudo stacking velocity model (V_{pseudo}) with units of years per nanosecond by dividing the age-travel-time model by the two-way travel times. Then we converted the radar image from travel-time to the Wheeler domain by a vertical stretch using V_{pseudo} (Fig. S.4). We oversampled

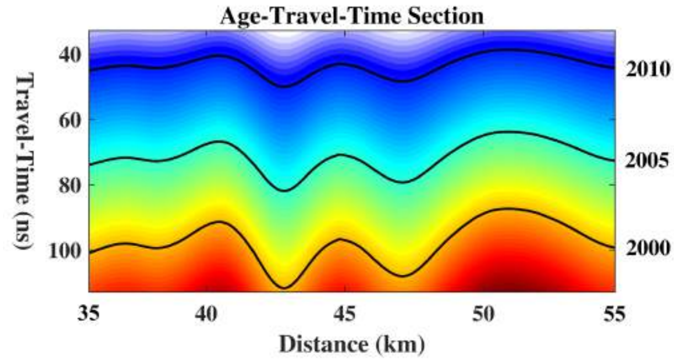

Fig. S.3: The age-travel-time model was calculated from pseudo velocities. Contours of this image are isochronous travel-time horizons. January 1, 2010, 2005, and 2000 are labeled for reference. We used the age-travel-time model to flatten the radar traces, by converting the time domain image into the age domain (Fig. S.4).

in the Wheeler domain to prevent signal aliasing. The age converted radargram has approximately flattened stratigraphy, such that any row of the image is isochronous. If we knew the structure orientation perfectly, and radar isochrones truly had the same age, the layers in the Wheeler domain would be theoretically flat. By picking, we calculated the residual age of five IRHs with an average epoch of 5.3 ± 2.7 years (the latest being the 1991 horizon) and used 1D shape preserving piecewise interpolation polynomials (Kahaner and others, 1989) to create a grid of perturbations for the age-travel-time model (Fig. S.5). Perturbations beyond the last picked horizon were set to zero. We applied the perturbations to the age model and re-flattened the image by stretching the traces to the updated age model (Fig. S.6). Radar amplitudes are now approximately horizontal across each row of the Wheeler domain image, indicating that the age-travel-time model fits the firn structure and IRH theory.

We applied the fx-deconvolution noise suppression algorithm (Gulunay, 1986) to the Wheeler domain radargram (Fig. S.7). Fx-deconvolution relies on autoregression modeling of the GPR signal in the frequency domain to build the optimal complex Wiener filter (Treitel, 1974). We applied the filter by averaging overlapping computations along the age axis to alleviate non-stationarity of the signal frequency. This process can benefit any GPR imagery of polar firn, provided that an initial stratigraphic age model, as a proxy for the structure, and methods to convert the image domain are available. At GTC15 Spur West, due to the large spatial gradient in SMB, it was necessary to determine the model residual and re-flatten the image before filtering. For GPR imagery expressing small or gradual SMB variability it may be sufficient to apply the structure-oriented filter without residual corrections to the Wheeler image.

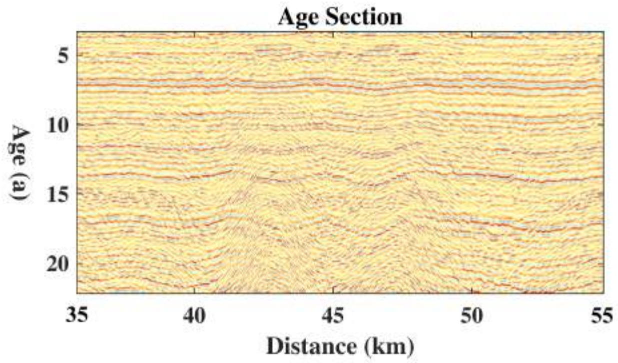

Fig. S.4: Using the initial age model, the Wheeler domain radargram has minor remnant undulations. Because the rows of the Wheeler image are isochronous, the undulations that deviate from row-wise horizontal are the model residual. If the age model was correct the radar reflections would be entirely horizontal (Fig. S.6). By interpreting five horizons of this image, we interpolated the model residual (Fig. S.5) and applied these perturbations to update the age model such that it is accurate in a relative sense.

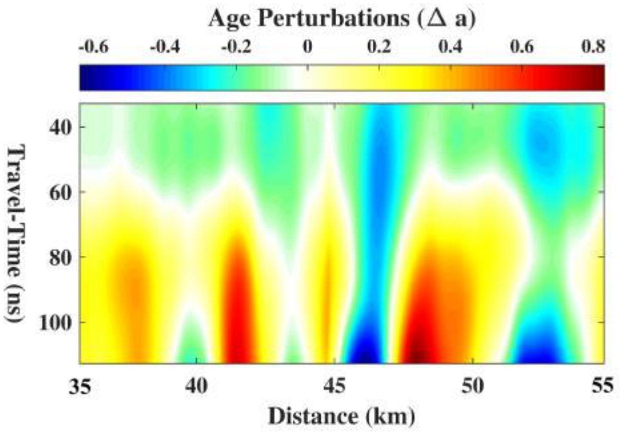

Fig. S.5: Perturbations in the travel-time domain are calculated by picking IRHs in Fig. S.4. When applied, the Wheeler domain image is reflattened (Fig. S.6), which ensures that the age model is accurate in a relative sense. We rely on ages measured from the firn core for absolute accuracy in the age model.

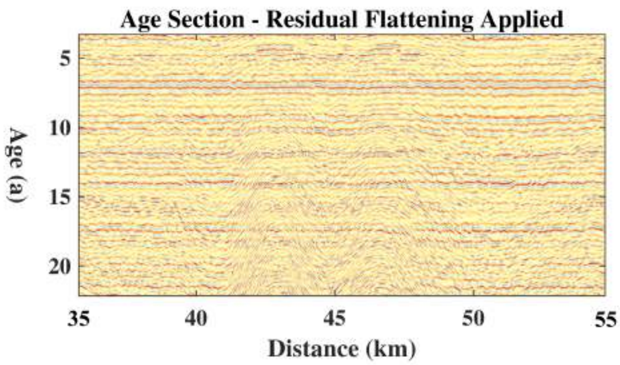

Fig. S.6: After interpreting five horizons of Fig. S.4, calculating the model residual (Fig. S.5), and applying the perturbations to the age-travel-time model (Fig. S.3), we re-flattened the Wheeler image. The radar amplitudes are now approximately horizontal, indicating that the updated age model is accurate according to the IRH theory.

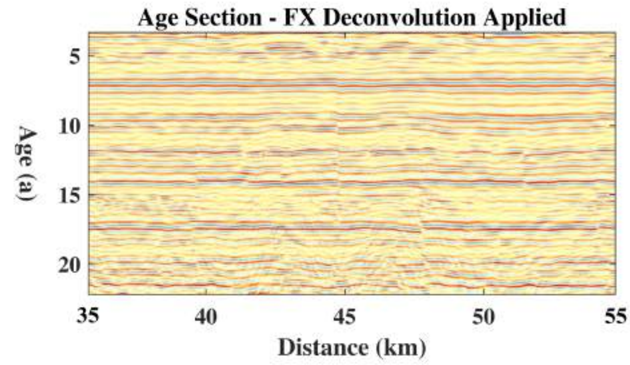

Fig. S.7: Flattening the traces improves their predictability by linear modeling. We applied the fx-deconvolution algorithm (Gulunay, 1986) to suppress the random noise that contaminates the linearly predictable signal.

S.1.7. Depth Imaging for Model Updates

We converted the updated age-travel-time model to depth using the stacking velocity model and then we used the age-depth model to convert the Wheeler domain image to depth. We applied a vertical stretch for each conversion operation (Margrave and Lamoureux, 2019). Figure 8 reveals the smooth and continuous IRHs of the depth image. The additional step of structure-oriented filtering extended the interpretable isochrone record from 1991 to 1984 (which is only limited by the time-window range of the radar acquisition). We picked 16 IRHs on the depth image with an average epoch of 2.1 ± 1.7 years. Over an equivalent depth range, this compares to the seven IRHs at five year age resolution used by Lewis and others (2019) to estimate SMB along GTC15 Spur West. In the vicinity of GTC15 the residuals between the GTC15 age-depth scale and the picked IRH ages were calculated. We created a second set of age perturbations using 1D linear interpolation with linear extrapolation to estimate perturbations beyond the deepest picked IRH (Fig. S.8), and we applied these perturbations to update the age-depth model. We then used the updated age model to calculate the instantaneous SMB.

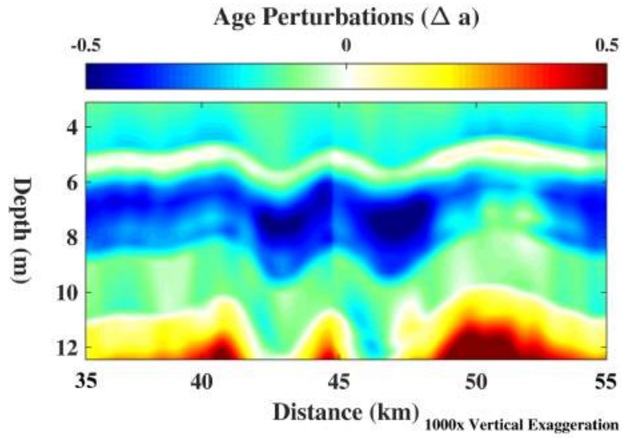

Fig. S.8: We interpreted 16 IRHs of Fig. 8 to measure their relative age at depth. We calculated the residual between our interpreted ages and the ages measured from GTC15 and interpolated this grid of perturbations in the depth domain. We applied these perturbations to the age-depth model which was used to calculate the SMB time-series. Applying this set of perturbations makes the relative age-depth model accurate in an absolute sense.

REFERENCES

Arcone SA, Spikes VB, Hamilton GS and Mayewski PA (2004) Stratigraphic continuity in 400 MHz short-pulse radar profiles of firn in West Antarctica. *Ann. Glaciol.*, **39**(2002), 195–200, ISSN 02603055 (doi: 10.3189/172756404781813925)

Arcone SA, Spikes VB and Hamilton GS (2005) Stratigraphic variation within polar firn caused by differential accumulation and ice flow: Interpretation of a 400 MHz short-pulse radar profile from West Antarctica. *J. Glaciol.*, **51**(174), 407–422, ISSN 00221430 (doi: 10.3189/172756505781829151)

Aster RC, Borchers B and Thurber CH (2019) *Parameter estimation and inverse problems.* Elsevier

Birkel S (2018) Greenland surface mass balance derived from climate reanalysis models, 1979-2017 (doi: 10.18739/A2D21RH75)

Businger P and Golub GH (1965) Linear least squares solutions by householder transformations. *Numer. Math.*, **7**(3), 269–276, ISSN 0029-599X (doi: 10.1007/BF01436084)

Dorn GA (1998) Modern 3-D seismic interpretation. *Lead. Edge*, **17**(9), 1262–1262, ISSN 1070-485X (doi: 10.1190/1.1438121)

Efron B and Stein C (1981) The Jackknife Estimate of Variance. *Ann. Stat.*, **9**(3), 586–596, ISSN 0090-5364 (doi: 10.1214/aos/1176345462)

Efron B and Tibshirani R (1986) Bootstrap Methods for Standard Errors, Confidence Intervals, and Other Measures of Statistical Accuracy. *Stat. Sci.*, **1**(1), 54–77, ISSN 0883-4237, 2168-8745 (doi: 10.1214/ss/1177013815)

Fehmers GC and Höcker CF (2003) Fast structural interpretation with structure-oriented filtering. *Geophysics*, **68**(4), 1286–1293, ISSN 00168033 (doi: 10.1190/1.1598121)

Fornberg B (1988) Generation of Finite Difference Formulas on Arbitrarily Spaced Grids. *Math. Comput.*, **51**(184), 699, ISSN 00255718 (doi: 10.2307/2008770)

Green CH (1938) Velocity Determinations by Means of Reflection Profiles. *Geophysics*, **3**(4), 295–305, ISSN 0016-8033 (doi: 10.1190/1.1439508)

Gulunay N (1986) FXDECON and complex wiener prediction filter. In *SEG Tech. Progr. Expand. Abstr. 1986*, 279–281, Society of Exploration Geophysicists (doi: 10.1190/1.1893128)

Herron MM and Langway CC (1980) Firn Densification: An Emperical Model. *J. Glaciol.*, **25**(93), 373–385, ISSN 00221430

Kahaner D, Moler C and Nash S (1989) Numerical methods and software. *Englewood Cliffs Prentice Hall, 1989*

Karimi P and Fomel S (2015) Stratigraphic coordinates: A coordinate system tailored to seismic interpretation. *Geophys. Prospect.*, **63**(5), 1246–1255, ISSN 13652478 (doi: 10.1111/1365-2478.12224)

Lewis G, Osterberg E, Hawley R, Marshall HP, Meehan T, Graeter K, McCarthy F, Overly T, Thundercloud Z and Ferris D (2019) Recent precipitation decrease across the western Greenland ice sheet percolation zone. *Cryosph.*, **13**(11), 2797–2815, ISSN 1994-0424 (doi: 10.5194/tc-13-2797-2019)

Loewe F (1970) Screen Temperatures and 10m Temperatures. *J. Glaciol.*, **9**(56), 263–268, ISSN 0022-1430 (doi: 10.3189/S0022143000023571)

Margrave GF and Lamoureux MP (2019) *Numerical Methods of Exploration Seismology.* Cambridge University Press, ISBN 9781316756041 (doi: 10.1017/9781316756041)

Nelder JA and Mead R (1965) A Simplex Method for Function Minimization. *The Computer Journal*, **7**(4), 308–313, ISSN 0010-4620 (doi: 10.1093/comjnl/7.4.308)

Ng F and King EC (2011) Kinematic waves in polar firn stratigraphy. *J. Glaciol.*, **57**(206), 1119–1134, ISSN 0022-1430 (doi: 10.3189/002214311798843340)

Rupper S, Christensen WF, Bickmore BR, Burgener L, Koenig LS, Koutnik MR, Miège C and Forster RR (2015) The effects of dating uncertainties on net accumulation estimates from firn cores. *J. Glaciol.*, **61**(225), 163–172, ISSN 00221430 (doi: 10.3189/2015JoG14J042)

Spikes VB, Hamilton GS, Arcone SA, Kaspari S and Mayewski PA (2004) Variability in accumulation rates from GPR profiling on the West Antarctic plateau. *Ann. Glaciol.*, **39**, 238–244, ISSN 02603055 (doi: 10.3189/172756404781814393)

Treitel S (1974) THE COMPLEX WIENER FILTER. *GEOPHYSICS*, **39**(2), 169–173, ISSN 0016-8033 (doi: 10.1190/1.1440419)

Ulaby FT, Fung AK and Moore RK (1986) *Microwave remote sensing: active and passive*, volume 3 of *From Theory to Applications*. Artech House

Wharton RP, Hazen GA, Rau RN and Best DL (1980) Advancements In Electromagnetic Propagation Logging. In *SPE Rocky Mt. Reg. Meet.*, Society of Petroleum Engineers, Society of Petroleum Engineers (doi: 10.2118/9041-MS)

Wheeler HE (1958) Time-Stratigraphy. *Am. Assoc. Pet. Geol. Bull.*, **42**(5), 1047–1063, ISSN 0149-1423 (doi: 10.1306/0BDA5AF2-16BD-11D7-8645000102C1865D)

Yilmaz Ö (2001) *Seismic Data Analysis*. Society of Exploration Geophysicists, ISBN 978-1-56080-094-1 (doi: 10.1190/1.9781560801580)